



Finite element modelling of concrete-filled double-skin steel stiffened tubular chord-to-SHS steel brace T-joints: Behaviour and design

Yan Diao^a, Jun Wang^a, Hongzhi He^a, M.F. Hassanein^{a,b,*}, Yong-Bo Shao^a, K.A. Cashell^c, A.Y. Elghazouli^{d,e}

^a School of Architecture and Civil Engineering, Xihua University, Chengdu 610039, PR China

^b Department of Structural Engineering, Faculty of Engineering, Tanta University, Tanta, Egypt

^c Department of Civil Environmental and Geomatic Engineering, UCL, London, UK

^d Dept. of Civil & Environmental Engineering, Hong Kong Polytechnic University, Hong Kong

^e Dept. of Civil & Environmental Engineering, Imperial College London, UK

ARTICLE INFO

Keywords:

Tubular T-joints
Concrete-filled steel tubes
Numerical modelling
Design procedures

ABSTRACT

Although concrete-filled double-skin stiffened steel tubular (CFDSST) members have been researched and applied in recent years, their use in truss T-joints has been lacking. This paper therefore examines the mechanical behaviour of CFDSST chord-to-hollow steel section (SHS) brace T-joints under axial brace loading. Detailed finite element models for CFDSST-to-SHS T-joints are firstly validated by assessing the modelling approaches against recent tests for CFDSST columns and other types of T-joints. The models are subsequently used to conduct parametric assessments into the influence of key factors, including the brace-to-chord width ratio, brace-to-chord thickness ratio, material strengths, hollow ratio of CFDSST chord, and the axial load applied on the chord. It is shown that the ultimate load capacity of the T-joints increases with the increase in the brace-to-chord width ratio as well as with higher steel tube and sandwiched concrete material strength, with a much less pronounced influence from the brace-to-chord thickness ratio. A new parameter representing the flexural stiffness-to-member length ratio of the chord to the brace is also introduced, based on which the failure modes are separated into two categories related to either the failure of the brace or of the chord. Using the detailed results and observations, existing methods for determining the bearing capacities of T-joints are evaluated, leading to the development of a new design approach. The proposed design procedure is shown to provide accurate predictions for CFDSST-to-SHS T-joints, indicating its suitability for use in practical application.

1. Introduction

Compared to steel and concrete members, concrete-filled steel tubular (CFST) elements provide improved performance in terms of stiffness, capacity, ductility, fire resistance, and seismic behaviour because due to the combined benefits of both materials [1,2]. The Ganhaizi extra-large bridge (Fig. 1(a)) is an example of the numerous modern structural engineering applications for traditional CFST structures, which include bridges and tall buildings [3]. More recently, to improve the performance of CFST, use has been made of high and ultra-high-strength materials [4], stiffeners [5,6], and inner steel tubes [7,8]. By adding stiffeners, concrete-filled stiffened steel tubular (CFSSST) columns, such as shown in Fig. 1(b), have provided higher

strength compared to conventional CFST members [5,6,9]. Moreover, concrete-filled double-skin steel tubular (CFDST) members, formed from two concentrically placed steel tubes, with concrete infill in-between, have been examined and adopted in practice [10–12], as shown in Fig. 1(c). Importantly, CFDST possesses the merits of CFST members, but with less weight as well as improved fire resistance as the inner steel tube is protected by the surrounding concrete.

Concrete-filled double-skin stiffened steel tubular (CFDSST) members are a relatively recent development and are fabricated as illustrated in Fig. 2. Four lipped angles of cold-formed plates are typically welded to form the outer steel tube and stiffeners at the same time, with a square or circular steel tube employed as an inner tube. The final composite cross-section can, however be used in two forms: (i) concrete-filled dual steel

* Corresponding author at: School of Architecture and Civil Engineering, Xihua University, Chengdu 610039, PR China.

E-mail addresses: yandiao@xhu.edu.cn (Y. Diao), wangjun2@stu.xhu.edu.cn (J. Wang), hehongzhi@stu.xhu.edu.cn (H. He), mostafa.fahmi@f-eng.tanta.edu.eg (M.F. Hassanein), shaoyb@mail.xhu.edu.cn (Y.-B. Shao), k.cashell@ucl.ac.uk (K.A. Cashell), a.elghazouli@imperial.ac.uk (A.Y. Elghazouli).

<https://doi.org/10.1016/j.engstruct.2025.119858>

Received 13 December 2024; Received in revised form 16 January 2025; Accepted 2 February 2025

Available online 19 February 2025

0141-0296/© 2025 The Author(s). Published by Elsevier Ltd. This is an open access article under the CC BY license (<http://creativecommons.org/licenses/by/4.0/>).

tubular (CFDT) form, which has both sandwiched concrete and core concrete, and (ii) concrete-filled double-skin steel tubular (CFDSST) form, which only has sandwiched concrete. They have the same benefits as conventional CFST members, but perform better under axial loading [13,14], eccentric loading [15], at both ambient and elevated temperatures [16]. Recent investigations have focused on the behaviour of stocky and slender CFDSST columns [17–21], and demonstrated their favourable mechanical properties.

T-joints represent a common form of brace to column connections. Several previous studies have assessed the behaviour of CFDT and CFST T-joints, as these regularly form important components in truss bridges, such as the Ganhaizi bridge, see Fig. 1(a). Through testing and numerical analysis, Diao et al. [22] examined the behaviour of CFST chord with PBL stiffeners-to-SHS brace T-joints. The behaviour of the T-joint with CFDT chord-to-SHS brace was also investigated by Yang et al. [23], from which the T-joint with CFDT chord was found to have enhanced performance relative to T-joints with CFST or SHS chords. The influence of various parameters on the bearing capacity of a rectangular CFST T-joint was also investigated by Li et al. [24]. In addition, Ma et al. [25] investigated the axial stiffness of CFST truss joints, and provided relationships for determining the axial stiffness of concrete filled rectangular steel tubular (CFRST) T, Y and K joints, which were adopted to predict the flexural stiffness of CFRST trusses. In contrast, no research has examined the application of CFDSST members in T-joints, which are formed by welding a SHS brace at the centre of a CFDSST chord. As the brace is subjected to axial loading, the bending capacity of the chord has a significant influence on the load carrying capacity of the T-joint. It is also noteworthy that, compared to CFDT, if the core concrete in the inner steel tube is removed in CFDSST chords, the self-weight reduces and the bending capacity is not notably affected due to the proximity of the infill to the neutral axis, which is examined in this paper through strength and strength-to-weight ratio comparisons.

This paper focuses on assessing the behaviour of novel CFDSST-to-SHS T-joints of the form shown in Fig. 3, which have not previously been studied. Detailed finite element (FE) models are constructed and validated by assessing the modelling procedures against recent tests on CFDSST columns and other types of T-joints (e.g. concrete filled steel tube (CFST) with PBL stiffeners chord-to-SHS brace T-joints). The models are then used to conduct parametric assessments into the influence of key factors on the behaviour, in order to address the lack of experimental data and gain detailed insights into the mechanical properties of this type of joint. The parameters considered include the brace-to-chord width ratio, brace-to-chord thickness ratio, material strengths,

hollow ratio of CFDSST chord, and the axial load applied on the chord. Using the detailed results and observations, existing methods for determining the bearing capacities of T-joints are evaluated, leading to the development of a new proposed design approach.

2. Numerical modelling

The nonlinear analysis program ABAQUS [26] was used to develop the finite element (FE) models used for simulating and investigating the response of CFDSST-SHS T-joints. This section outlines the procedure for constructing the FE models and the validation studies carried out by comparison against available experimental data.

2.1. Material models

2.1.1. Structural steel

The study of Tao et al. [27] showed that the ultimate strength of CFST columns was not significantly affected by the adopted material models for steel. For CFDSST columns, Wang et al. [17] employed an elastic-perfectly plastic steel model and strain hardening was not accounted for. However, in T-joints, as the brace is under axial load and the chord is in bending, Diao et al. [22] indicated the importance of using a more representative model, and adopted an elastic-plastic material constitutive model for steel, as shown in Fig. 4, which is also employed in this paper. Four piece-wise linear segments are in the stress-strain relationship, namely: oa , ab , bc , and cd , which represent elastic, yielding, strain hardening, and ultimate strength, respectively. The strain ϵ_1 represents the initiation of yielding, ϵ_2 ($\epsilon_2 = 10\epsilon_1$) represents the start of hardening, ϵ_3 ($\epsilon_3 = 10\epsilon_2$) corresponds to the ultimate strength. The parameters f_y and f_u in Fig. 4 represent the yield strength and ultimate strength of steel, respectively. Young's modulus E_s is assumed as 206 GPa according to the Chinese design standard [28].

2.1.2. Concrete material model

In the joint configuration considered, as the brace is under axial load, the CFDSST chord will undergo bending and the concrete in the compression side of the section will be confined by the steel tubes. This is similar to square CFDSST slender columns [29], where the confinement effect of the steel tube improves the strength of CFDSST columns. Accordingly, the stress-strain relationship (given by Eq. 1) proposed by Tao et al. [27], was adopted to simulate the compressive behaviour of the confined concrete, as shown in Fig. 5, where σ and ϵ are the stress and strain, respectively, f'_c is the concrete cylinder compressive strength

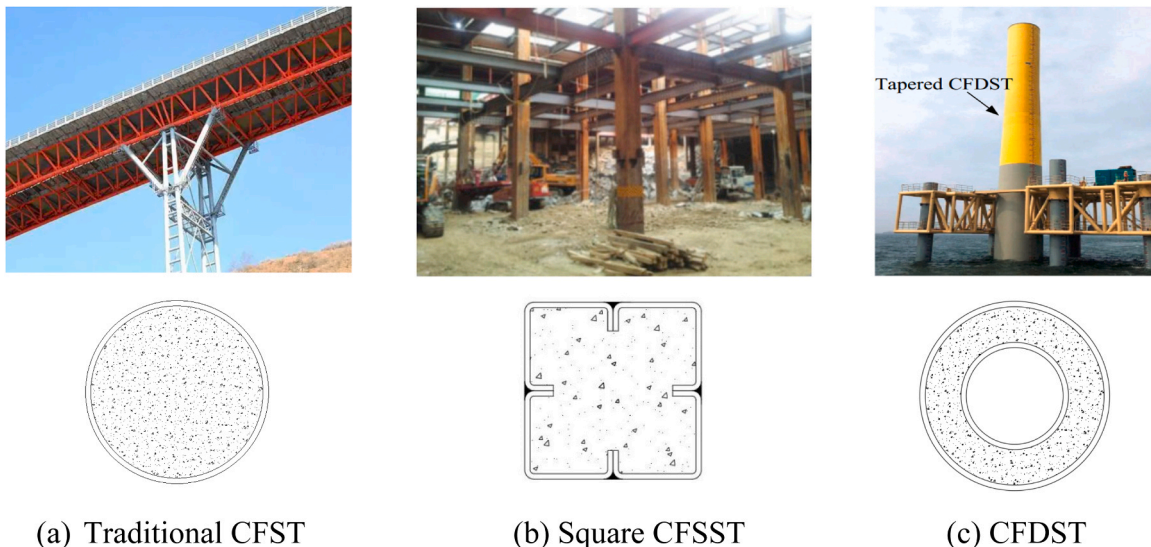


Fig. 1. Examples of applications for steel-concrete composite members.

taken as $0.79f_{cu}$ with f_{cu} being the concrete cubic compressive strength, f_r is the residual stress, assumed as $0.1f'_c$, and E_c is the elastic modulus of the concrete, considered as $4700\sqrt{f'_c}$.

$$\sigma = \begin{cases} \frac{AX + BX^2}{1 + (A - 2)X + (B + 1)X^2} f'_c & 0 < \varepsilon \leq \varepsilon_{c0} \\ f'_c \varepsilon_{c0} & f'_c \varepsilon_{c0} < \varepsilon \leq \varepsilon_{cc} \\ f_r + (f'_c - f_r) \exp\left[-\left(\frac{\varepsilon - \varepsilon_{cc}}{\alpha}\right)^m\right] & \varepsilon \geq \varepsilon_{cc} \end{cases} \quad (1)$$

where $X = \varepsilon/\varepsilon_{c0}$, $A = E_c \varepsilon_{c0}/f'_c$ and $B = (A - 1)^2/0.55 - 1$.

In Eq. 1, α is a parameter based on ξ_c , which is the confinement factor of the CFST, and both are expressed using Eq. 2 and Eq. 3, respectively:

$$\alpha = 0.005 + 0.0075\xi_c \quad (2)$$

$$\xi_c = \frac{A_s f_y}{A_c f_{ck}} \quad (3)$$

where A_s and f_y are the cross-sectional area and yield strength of the steel tube, respectively; A_c and f_{ck} ($= 0.67f_{cu}$) are the cross-sectional area and characteristic strength of concrete, respectively; ε_{c0} and ε_{cc} are expressed by Eq. 4 to Eq. 7, as follows:

$$\varepsilon_{c0} = 0.00076 + \sqrt{(0.626f'_c - 4.33) \times 10^{-7}} \quad (4)$$

$$\varepsilon_{cc} = \varepsilon_{c0} e^k \quad (5)$$

$$k = (2.9224 - 0.00367f'_c) \left(\frac{f_B}{f'_c}\right)^{0.3124 + 0.002f'_c} \quad (6)$$

$$f_B = \frac{0.25 \cdot (1 + 0.027f_y) \cdot e^{-0.02\sqrt{B^2 + D^2}/t}}{1 + 1.6e^{-10} \cdot (f'_c)^{4.8}} \quad (7)$$

where m is a model parameter, taken as 0.92.

2.2. Modelling procedure

Fig. 6 illustrates the T-joint model, which is made up of the core concrete, sandwiched concrete, inner and outer steel tubes, and brace element. To increase the computational efficiency, shell elements (S4R) were used for the steel tubes and eight-node brick elements (C3D8R) were employed for the concrete. Based on mesh sensitivity analysis, as used in a previous work [29], the mesh size was chosen as roughly one-tenth of the section size. Moreover, the interaction between the steel and the concrete was modelled using a "surface-to-surface contact," with a Mohr-Coulomb friction model with a coefficient of 0.6 in the tangential direction and a "hard contact" in the normal direction to permit

separation under tensile stress [6,27]. As illustrated in Fig. 6, the boundary conditions comprised hinges at both chord ends, with the translational degrees of freedom restricted perpendicular to the axial direction, while an axial load is applied to the brace. It is noteworthy that because the effect of residual stresses due to welding and corner strengthening on the behaviour and strength of CFDSST columns was found to be relatively low [30], residual stresses were not incorporated into the FE model. Moreover, no steel fracture was found in the corners and welds of the test specimens, thus ensuring that the welds had no effect on the strength and behaviour of CFDSST columns [30].

2.3. Validation studies

Available test data for CFDSST members and conventional T-joints was used for validation of the FE models, as there is currently no test data for CFDSST chord-to-SHS brace T-joints. The following tasks were carried out as part of this validation exercise: (i) The steel and concrete material models were validated using CFDSST short columns with inner square tubes [30,31], as these columns fail due to cross-sectional capacity rather than overall buckling; (ii) the bending behaviour of the chord in T-joints was verified using slender CFST columns with curling stiffeners [19]; and (iii) T-joints with CFST chords, including longitudinal [22] and diagonal stiffeners [23], were validated against experimental data to ensure that the FE models adequately capture the main behavioural characteristics.

The geometrical properties of the specimens are shown in Table 1. Apart from PBL-3 and TDP6, the specimens used in the validation were members subjected to axial compressive loading. In the table, B_0 and t_0 are the width and thickness of outer steel tube, respectively, B_1 (D) and t_1 are the width (diameter) and thickness of the inner steel tube, respectively, and L is the length of the columns or the chords of the T-joints. The test ultimate loads (N_{Exp}) and those predicted by the FE model (N_{FE}) in the case of T-joints were taken as the load applied to the brace, while for the columns, the test and FE ultimate values were their ultimate loads directly. The validation involved comparing the load-displacement curves as well as the failure modes.

Figs. 7–9 and Table 1 show the comparison between the experimental results and numerical results. The N_{FE}/N_{Exp} ratio indicates close agreement between test and numerical strengths, with an average of 0.98 and a standard deviation of 0.015, as shown in Table 1. However, some discrepancy is observed in terms of stiffness for Specimens CFST1 and CCFST1–2 tested by Wang et al [19], which is attributed to the idealisation of the boundary conditions and the assumed concrete stiffness. The load-displacement curves (Fig. 7) and failure modes (Fig. 8 and Fig. 9) demonstrate that the FE models faithfully represent the experimental behaviour, including local buckling and large bending deformations. As shown in Fig. 8, the FE model accurately depicted the overall buckling of the slender column CCFST1–2 [19] and the local buckling of the CFDSST short column SS-160–1 [30] as those obtained

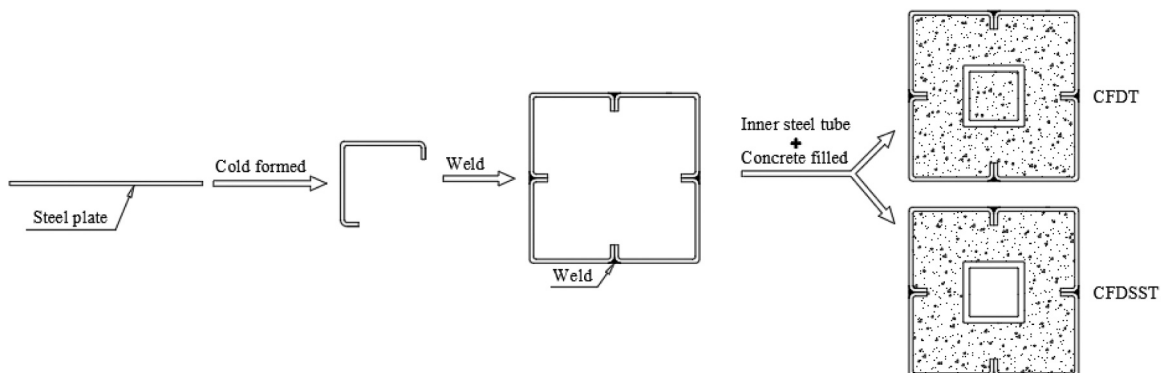
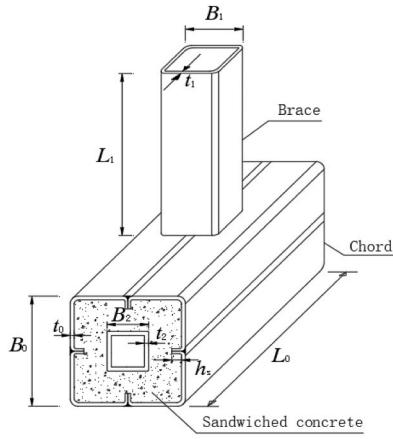
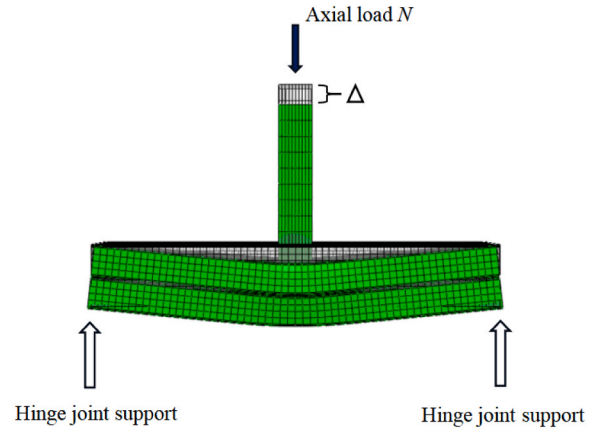


Fig. 2. Fabrication process of CFDSST.



(a) 3D diagram



(b) Deformation under axial load

Fig. 3. Typical CFDSST-to-SHS T-joint and deformation under load.

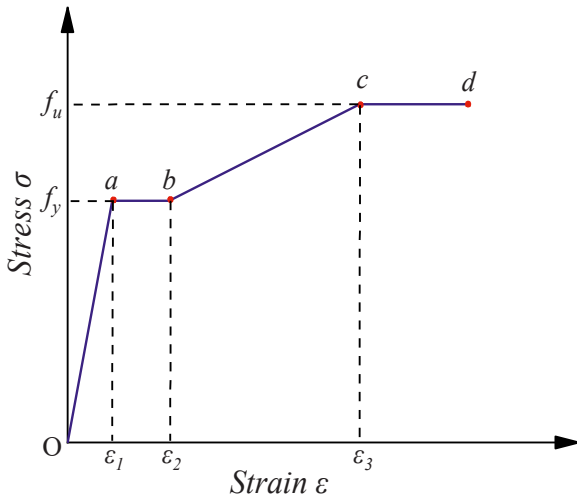


Fig. 4. Stress-strain relationship for steel [22].

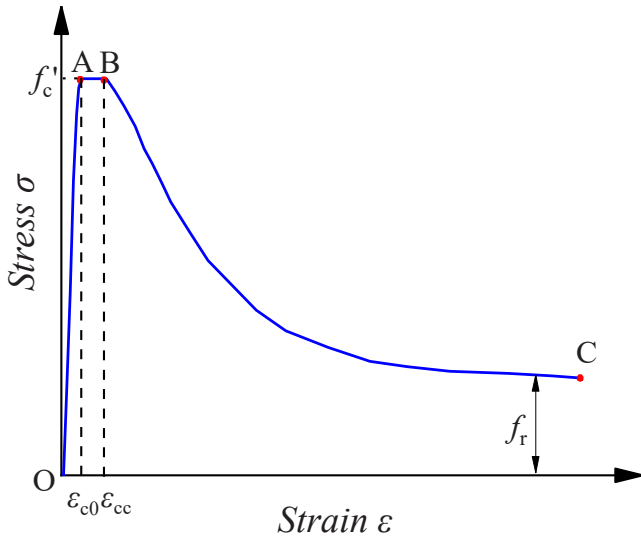


Fig. 5. Stress-strain relationship for concrete [27].

experimentally. Moreover, as Fig. 9 illustrates, the substantial bending deformations of the chord of T-joints PBL-3 and TDP6 are also captured well by the analysis. Overall, these validations indicate that the FE models, which are used to examine the behaviour of CFDSST chord-to-SHS brace T-joints utilizing specimens PBL-3 [22] and TDP6 [32] can be reliably used in examining the behaviour and strength of the CFDSST chord-to-SHS brace T-joints.

3. Parametric assessments

In this section, several parametric studies were generated to assess the behaviour and strength of CFDSST-to-SHS T-joints. A total of 92 finite element (FE) simulations covering a range of parameter variations were established in order to address the lack of experimental data and gain a better understanding of the mechanical properties of these joints. Table 2 provides the details of these FE models. The 3D schematic of the CFDSST-to-SHS T-joint shown in Fig. 3(a) defines the different geometric characteristics. The key parameters examined include the brace-to-chord width ratio ($\beta = 0.5 \sim 1.0$), brace-to-chord thickness ratio ($\tau = 0.83 \sim 2.00$), concrete strength ($f_c = 40 \sim 80 \text{ MPa}$), steel yield strength ($f_y = 235 \sim 460 \text{ MPa}$), chord stiffener depth ($h_s = 20 \sim 70 \text{ mm}$), and axial load on the chord relative to its capacity [31] ($\frac{N}{N_{c,ult}} = 0.0 \sim 0.6$). The chord length-to-width ratio (L_0/B_0) was varied between 5.56 and 7.50, while the SHS length-to-width ratio (L_1/B_1) ranged from 2.50 to 5.00. The slenderness ratio of the chord's outer tube ranged from 11.11 to 30.43, and this ranged from 5.56 to 35.00 for the SHS. The hollow ratio of the double-skin chord (χ) varied from 0.04 to 0.41. Due to the presence of the concrete infill, inward local buckling (LB) of the outer steel tubes of the chord is avoided when the brace is subjected to an axial compression force, while inward and outward LB is eliminated in the inner steel tubes. However, because the brace is devoid of concrete, standard width-to-thickness ratio restrictions are used, as determined from Eq. 8 following GB 50017–2017 [28]:

$$(B_1 - 2t_1) / t_1 \leq 40 \sqrt{\frac{235}{f_y}} \quad (8)$$

where λ is the slenderness ratio of the brace, and f_y is the yield strength of the steel for the brace. The overall resistance N_b is determined as given in Eq. 9 [28]:

$$N_b = \varphi A f_y \quad (9)$$

where A is the cross-sectional area of the brace and the stability coefficient (φ) is expressed as:

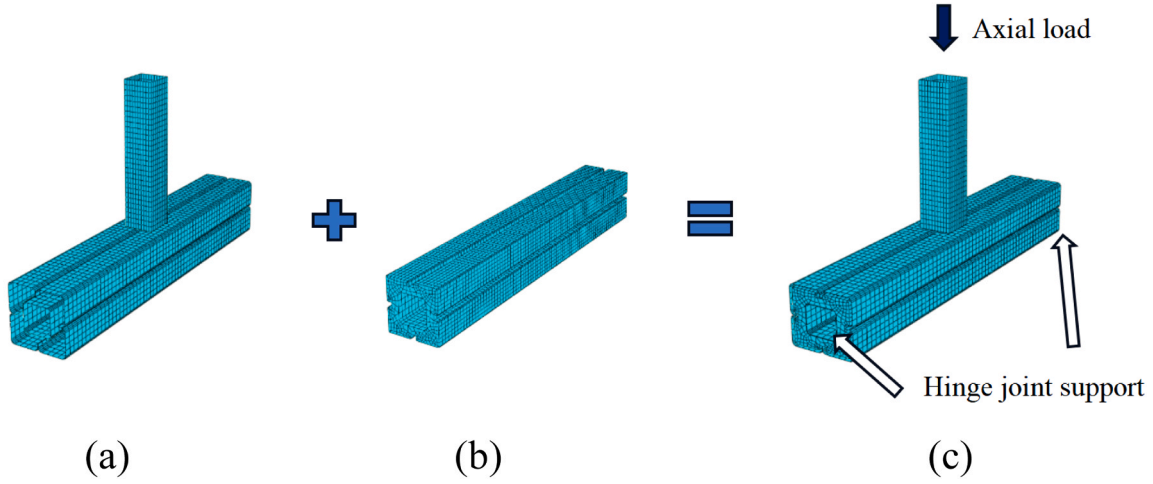


Fig. 6. Mesh, load application and boundary conditions for: (a) steel tubes, (b) concrete components, and (c) T-joint.

Table 1

Geometric properties and strengths of the test specimens used in the validation.

Ref.	Specimens	Type	B_0 (mm)	t_0 (mm)	B_1 (D) (mm)	t_1 (mm)	L (mm)	N_{Exp} (kN)	N_{FE} (kN)	N_{FE}/N_{Exp}
[31]	SS-180-2	Short column	180	2.0	80	4	540	2441	2404	0.98
[30]	SS-160-1	Short column	160	1.9	50	2.76	480	1728	1648	0.95
[19]	CFST1	Short column	160	2.1	-	-	1190	1344	1337	0.99
	CCFST1-2	Slender column	160	2.1	110	1.95	1190	2242	2190	0.98
[22]	PBL-3	T-joint	120	3.5	-	-	740	350	347	0.99
[32]	TDP6	T-joint	120	4.0	-	-	740	349	345	0.99
Average										0.98
Standard Deviation										0.015

$$\varphi = \begin{cases} 1 - \alpha_1 \bar{\lambda}^2 & (\bar{\lambda} \leq 0.215) \\ \frac{1}{2\bar{\lambda}^2} \left[\alpha_2 + \alpha_3 \bar{\lambda} + \bar{\lambda}^2 - \sqrt{(\alpha_2 + \alpha_3 \bar{\lambda} + \bar{\lambda}^2)^2 - 4\bar{\lambda}^2} \right] & (\bar{\lambda} \leq 0.215) \end{cases} \quad (10)$$

where α_1 , α_2 , and α_3 are coefficients obtained from Table 3 depending on the cross-section type. The type of cross-section is determined by its shape, dimensions, and the production method used (such as rolling, welding, or flame cutting). In this study, the brace is classified as Type b. On the other hand, $\bar{\lambda}$ is the normalized slenderness ratio, which is given as:

$$\bar{\lambda} = \lambda / \lambda_0 = \lambda \sqrt{f_y / E} / \pi \quad (11)$$

4. Main behavioural characteristics

4.1. Failure modes

The T-joint is composed of two primary elements: the brace and the chord. The strength relationship between these elements influences the failure mode of the joint. When the brace is in axial compression, it experiences compressive deformation while the chord is subjected to bending (refer to Fig. 3(b)). In this illustration, N indicates the load applied to the brace, and Δ represents the axial displacement at the top of the brace tube. A parameter K is introduced herein to predict the failure mode, which characterises the ratio of flexural stiffness relative to the lengths of the brace and chord members, and is represented as:

$$K = \frac{(E_1 I_1) / L_1}{(E_0 I_0) / L_0} \quad (12)$$

where L_1 and L_0 are the lengths of the brace and chord, respectively, and

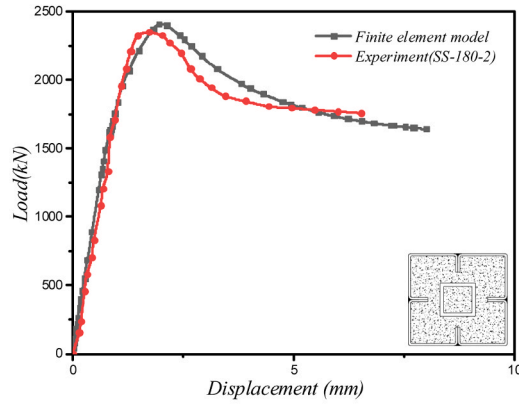
$E_1 I_1$ and $E_0 I_0$ are their corresponding flexural stiffnesses. It is noteworthy that a parameter like K has not previously been proposed in the available literature for T-joints of different configurations. The flexural stiffness of the chord is the sum of the stiffnesses of its constituent parts, with the concrete contribution reduced by 40 %, as per DBJ/T13-51-2010 [33]. Thus, the flexural stiffness of the chord can be expressed as:

$$E_0 I_0 = E_{so} I_{so} + E_{si} I_{si} + E_{ss} I_{ss} + 0.6(E_{cs} I_{cs} + E_{ci} I_{ci}) \quad (13)$$

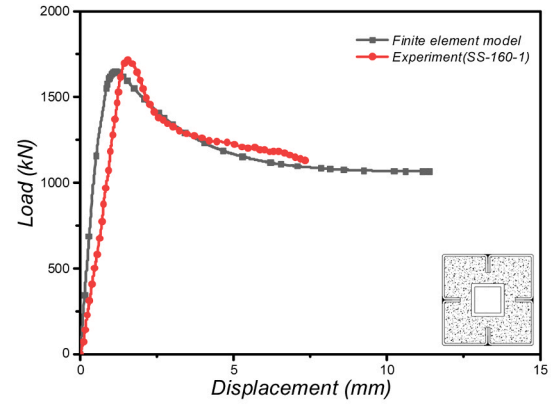
where E_{so} , E_{si} , E_{ss} , E_{cs} and E_{ci} are the moduli of elasticity of the outer steel tube, inner steel tube, stiffeners, sandwiched concrete, and core concrete, respectively. Similarly, I_1 , I_{so} , I_{si} , I_{ss} , I_{cs} and I_{ci} are the second moments of area of the cross-sections of the brace, outer steel tube, inner steel tube, stiffeners, sandwiched concrete, and core concrete, respectively.

Fig. 10 shows how parameter K affects the N_b / N_u^{FE} ratio, N_b is the compression resistance of the brace determined by Eq. 9 and N_u^{FE} is the ultimate axial compression load derived from the FE analysis. In addition, Table 4 shows the corresponding $N-\Delta$ curves, as well as the deformed shapes at maximum and final loads. The maximum load is specified in the following section for Models S1, which do not show a discernible descending segment in the later stages of their response curves. The maximum load for these models is assumed at a displacement of $L_0/50$. Based on the FE analysis, failure modes, and associated $N-\Delta$ curves, a failure mode boundary of $K = 0.18$ is proposed as represented by the straight-line trendline shown in Fig. 10.

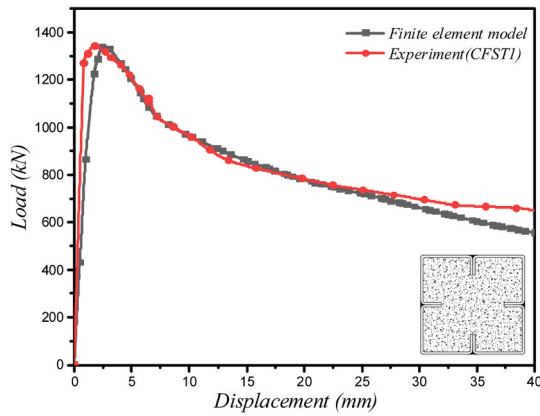
With ratios ranging from roughly 0.95–1.05, the values of N_b and N_u^{FE} to the left of $K = 0.18$ boundary are quite close. This implies that the calculated brace resistance and the joint total capacity are quite similar. This occurs because the brace, which controls the joint capacity, is weaker in specimens with $K < 0.18$ in relation to the chord. The differences between specimens with $K < 0.18$ and those with $K \geq 0.18$



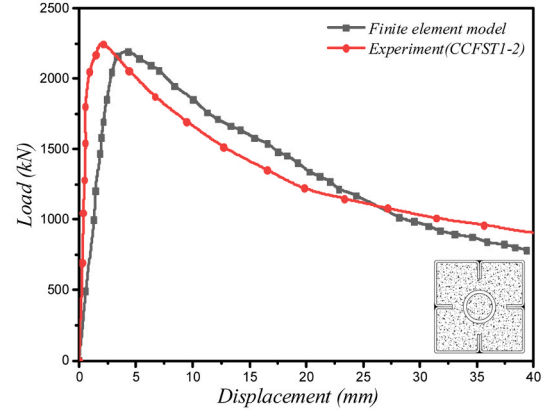
(a) SS-180-2



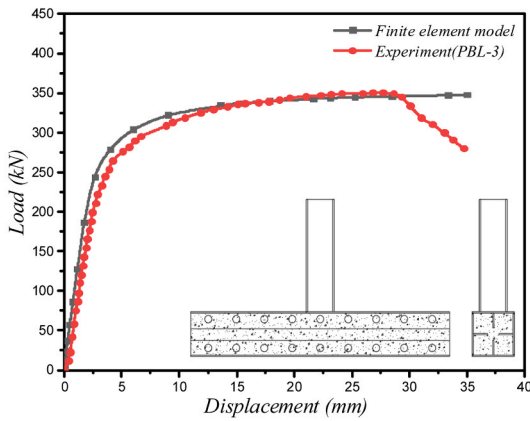
(b) SS-160-1



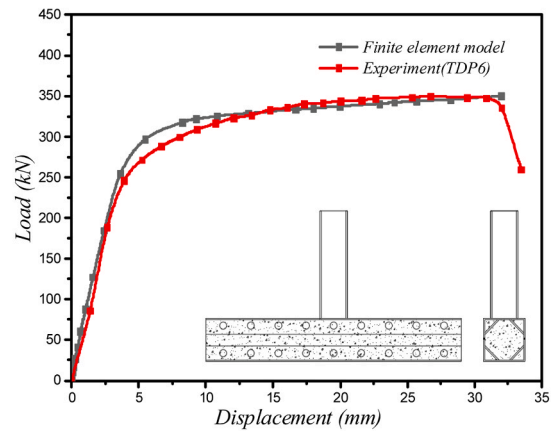
(c) CFST1



(d) CCFST1-2



(e) PBL-3



(f) TDP6

Fig. 7. Comparison of load-displacement curves obtained from tests and FE models.

become noticeable later on, especially in the final deformations and the $N-\Delta$ curves (as shown in Table 4), even if the deformations at maximum load are not considerably different. Specimens with $K < 0.18$ exhibit final deformations with minimal chord bending and significant local buckling failure in the brace, as indicated in Table 4(a). Model S102 clearly exhibits this failure mechanism ($K = 0.154$). The joint quick loss

of load-bearing capability as a result of bracing failure is indicated by the abrupt drop in the latter portion of the load-displacement curve. It is important to note that the failure mode changes when K approaches a value of 0.18, indicating that the brace flexural stiffness increases in relation to the chord, which is shown by S88($K = 0.176$) in Table 4(b).

On the other hand, $N_b > N_u^{FE}$ occurs to the right of the $K = 0.18$

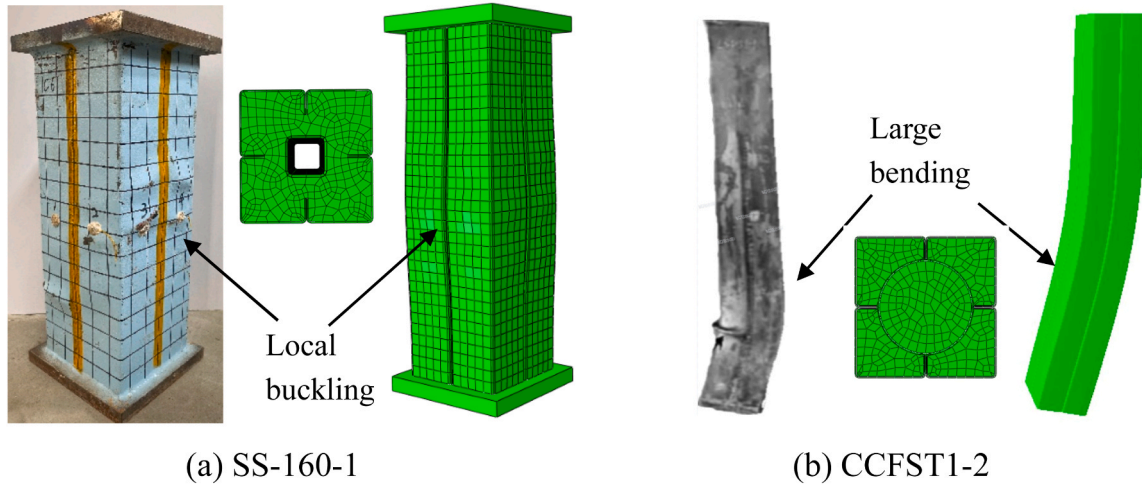


Fig. 8. Comparison of failure modes from tests and FE models for: (a) short column SS-160-1 [30] and (b) Slender column CCFST1-2 [19].

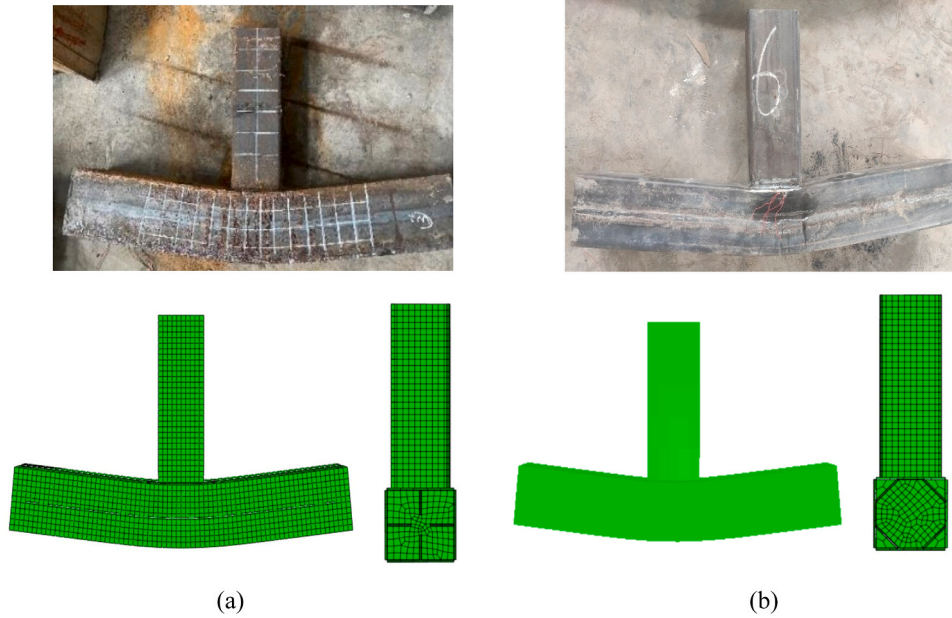


Fig. 9. Comparison of failure modes from tests and FE models for T-joints: (a) PBL-3 [22] and (b) TDP6 [32].

boundary in Fig. 10, suggesting that the brace does not fail before the T-joint reaches its ultimate load-bearing capability. Significant chord bending deformation without brace buckling is the main failure mode for T-joint models S97 and S1, as indicated in Table 4(c) and (d). In these situations, the primary role of the brace is to transfer the applied load, and the chord bending capacity determines the joint load-bearing capacity. Furthermore, there is no noticeable decreasing segment in the load-displacement curves for these models, indicating that the joint capacity to support loads has not been compromised and that the brace did not fail. These results show that when $K = 0.18$, the failure modes of CFDSST-to-SHS T-joints under axial compression of the brace vary. When K is less than 0.18, the CFDSST-to-SHS T-joint is governed by brace failure due to local buckling and overall instability; in contrast, when K is greater than 0.18, the chord fails through significant bending deformation.

4.2. Bearing capacity of T-joints

As discussed above, the load-displacement response of CFDSST-to-

SHS T-joints can be divided into two types based on the value of K , considering the results of the preceding section. This is illustrated in Table 4, where N_u^{FE} represents the ultimate load and Δ_u is the corresponding displacement. N_u^{FE} is the peak load the curve for the first response type, which occurs when $K < 0.18$ and the brace determines the joint bearing capacity, as shown in Table 4(a) and (b), which represents the load-displacement curve of T-joint S102(with $K = 0.154$) and S88(with $K = 0.176$), respectively. In this case, the joint bearing capacity N_u^{FE} is similar to the value of the brace computed resistance N_b . Therefore, N_b can be calculated using Eq. 9 to determine the bearing capacity of the CFDSST-to-SHS T-joint in cases when $K < 0.18$. On the other hand, when $K \geq 0.18$, the second type of load-displacement curve occurs, as presented in Table 4 (c) and (d) for T-joint S97(with $K = 0.184$) and S1(with $K = 0.203$), respectively. The most obvious distinction from the first curve type is the absence of a sharp decline in load because the brace does not fail in this case. The chord experiences considerable deformation in this situation and, although the FE models may replicate this behaviour, they do not depict the fracture or crack formation in the chord tube. A typical characteristic of FE models for

Table 2
Details for the parametric study on CFDSST-to-SHS T-joints.

Group	FE model	CFDSST chord member									SHS brace member				β	τ	χ	N_c (kN)	K	N_b (kN)	N_u^{FE} (kN)
		Outer steel tube and sandwiched concrete of chord						Inner steel tube and concrete core													
		B_0 (mm)	t_0 (mm)	L_0 (mm)	f_{c0} (MPa)	f_{y0} (MPa)	h_s (mm)	B_2 (mm)	t_2 (mm)	f_{y2} (MPa)	B_1 (mm)	t_1 (mm)	f_{y1} (MPa)	L_1 (mm)							
G1	S1	160	7.2	960	40	355	20	80	3	355	80	7.2	355	400	0.50	1.00	0.28	0	0.203	727	619
	S2	160	7.2	960	40	355	20	80	3	355	100	7.2	355	400	0.63	1.00	0.28	0	0.418	935	637
	S3	160	7.2	960	40	355	20	80	3	355	120	7.2	355	400	0.75	1.00	0.28	0	0.749	1142	659
	S4	160	7.2	960	40	355	20	80	3	355	140	7.2	355	400	0.88	1.00	0.28	0	1.221	1348	681
	S5	160	7.2	960	40	355	20	80	3	355	160	7.2	355	400	1.00	1.00	0.28	0	1.859	1554	673
G2	S6	180	7.6	1080	40	355	30	80	3	355	90	7.6	355	450	0.50	1.00	0.22	0	0.199	871	704
	S7	180	7.6	1080	40	355	30	80	3	355	112.5	7.6	355	450	0.63	1.00	0.22	0	0.409	1109	717
	S8	180	7.6	1080	40	355	30	80	3	355	135	7.6	355	450	0.75	1.00	0.22	0	0.731	1347	737
	S9	180	7.6	1080	40	355	30	80	3	355	157.5	7.6	355	450	0.88	1.00	0.22	0	1.189	1585	768
	S10	180	7.6	1080	40	355	30	80	3	355	180	7.6	355	450	1.00	1.00	0.22	0	1.808	1823	771
G3	S11	280	9.2	1680	40	355	40	80	3	355	140	9.2	355	700	0.50	1.00	0.08	0	0.199	1678	1343
	S12	280	9.2	1680	40	355	40	80	3	355	175	9.2	355	700	0.63	1.00	0.08	0	0.405	2101	1363
	S13	280	9.2	1680	40	355	40	80	3	355	210	9.2	355	700	0.75	1.00	0.08	0	0.719	2544	1393
	S14	280	9.2	1680	40	355	40	80	3	355	245	9.2	355	700	0.88	1.00	0.08	0	1.164	2988	1440
	S15	280	9.2	1680	40	355	40	80	3	355	280	9.2	355	700	1.00	1.00	0.08	0	1.762	3431	1424
G4	S16	160	3.6	960	40	355	20	80	3	355	80	3.6	355	400	0.50	1.00	0.25	0	0.180	383	364
	S17	160	3.6	960	40	355	20	80	3	355	80	4.5	355	400	0.50	1.25	0.25	0	0.218	472	367
	S18	160	3.6	960	40	355	20	80	3	355	80	5.4	355	400	0.50	1.50	0.25	0	0.252	559	368
	S19	160	3.6	960	40	355	20	80	3	355	80	6.3	355	400	0.50	1.75	0.25	0	0.284	644	369
	S20	160	3.6	960	40	355	20	80	3	355	80	7.2	355	400	0.50	2.00	0.25	0	0.314	727	369
G5	S21	280	4.6	1680	40	355	40	80	3	355	140	4.6	355	700	0.50	1.00	0.08	0	0.171	868	814
	S22	280	4.6	1680	40	355	40	80	3	355	140	5.75	355	700	0.50	1.25	0.08	0	0.208	1074	820
	S23	280	4.6	1680	40	355	40	80	3	355	140	6.9	355	700	0.50	1.50	0.08	0	0.244	1278	825
	S24	280	4.6	1680	40	355	40	80	3	355	140	8.05	355	700	0.50	1.75	0.08	0	0.278	1477	828
	S25	280	4.6	1680	40	355	40	80	3	355	140	9.2	355	700	0.50	2.00	0.08	0	0.309	1678	831
G6	S26	160	3.6	960	40	355	20	80	3	355	80	7.2	355	400	0.50	2.00	0.25	0	0.314	727	370
	S27	160	4.5	960	40	355	20	80	3	355	80	9	355	400	0.50	2.00	0.26	0	0.319	885	438
	S28	160	5.4	960	40	355	20	80	3	355	80	10.8	355	400	0.50	2.00	0.26	0	0.318	1034	503
	S29	160	6.3	960	40	355	20	80	3	355	80	12.6	355	400	0.50	2.00	0.27	0	0.314	1174	567
	S30	160	7.2	960	40	355	20	80	3	355	80	14.4	355	400	0.50	2.00	0.28	0	0.308	1305	626
	S31	160	3.6	900	40	355	20	80	3	355	80	7.2	355	400	0.50	2.00	0.25	0	0.294	727	391
	S32	160	3.6	1000	40	355	20	80	3	355	80	7.2	355	400	0.50	2.00	0.25	0	0.327	727	349
	S33	160	3.6	1100	40	355	20	80	3	355	80	7.2	355	400	0.50	2.00	0.25	0	0.360	727	315
	S34	160	3.6	1200	40	355	20	80	3	355	80	7.2	355	400	0.50	2.00	0.25	0	0.392	727	288
	S35	160	3.6	960	50	355	20	80	3	355	80	7.2	355	400	0.50	2.00	0.25	0	0.306	727	378
	S36	160	3.6	960	60	355	20	80	3	355	80	7.2	355	400	0.50	2.00	0.25	0	0.299	727	385
	S37	160	3.6	960	70	355	20	80	3	355	80	7.2	355	400	0.50	2.00	0.25	0	0.294	727	391
	S38	160	3.6	960	80	355	20	80	3	355	80	7.2	355	400	0.50	2.00	0.25	0	0.288	727	397
S39	160	3.6	960	40	235	20	80	3	235	80	7.2	235	400	0.50	2.00	0.25	0	0.314	485	265	
S40	160	3.6	960	40	420	20	80	3	420	80	7.2	420	400	0.50	2.00	0.25	0	0.314	857	423	
S41	160	3.6	960	40	460	20	80	3	460	80	7.2	460	400	0.50	2.00	0.25	0	0.314	936	456	
S42	160	3.6	960	40	355	25	80	3	355	80	7.2	355	400	0.50	2.00	0.25	0	0.309	727	382	
S43	160	3.6	960	40	355	30	80	3	355	80	7.2	355	400	0.50	2.00	0.25	0	0.305	727	393	
S44	160	3.6	960	40	355	35	80	3	355	80	7.2	355	400	0.50	2.00	0.25	0	0.302	727	405	
S45	160	3.6	960	40	355	20	60	3	355	80	7.2	355	400	0.50	2.00	0.13	0	0.322	727	365	
S46	160	3.6	960	40	355	20	70	3	355	80	7.2	355	400	0.50	2.00	0.19	0	0.319	727	368	
S47	160	3.6	960	40	355	20	90	3	355	80	7.2	355	400	0.50	2.00	0.32	0	0.309	727	369	
S48	160	3.6	960	40	355	20	100	3	355	80	7.2	355	400	0.50	2.00	0.41	0	0.303	727	363	

(continued on next page)

Table 2 (continued)

Group	FE model	CFDSST chord member									SHS brace member				β	τ	χ	N_c (kN)	K	N_b (kN)	N_u^{FE} (kN)
		Outer steel tube and sandwiched concrete of chord						Inner steel tube and concrete core			B_1 (mm)	t_1 (mm)	f_{y1} (MPa)	L_1 (mm)							
		B_0 (mm)	t_0 (mm)	L_0 (mm)	f_{c0} (MPa)	f_{y0} (MPa)	h_s (mm)	B_2 (mm)	t_2 (mm)	f_{y2} (MPa)											
G7	S49	160	3.6	960	40	355	20	80	2	355	80	7.2	355	400	0.50	2.00	0.26	0	0.320	727	353
	S50	160	3.6	960	40	355	20	80	4	355	80	7.2	355	400	0.50	2.00	0.24	0	0.308	727	387
	S51	160	3.6	960	40	355	20	80	5	355	80	7.2	355	400	0.50	2.00	0.23	0	0.303	727	403
	S52	160	3.6	960	40	355	20	80	3	355	80	7.2	355	400	0.50	2.00	0.25	149	0.314	727	366
	S53	160	3.6	960	40	355	20	80	3	355	80	7.2	355	400	0.50	2.00	0.25	299	0.314	727	360
	S54	160	3.6	960	40	355	20	80	3	355	80	7.2	355	400	0.50	2.00	0.25	598	0.314	727	341
	S55	160	3.6	960	40	355	20	80	3	355	80	7.2	355	400	0.50	2.00	0.25	897	0.314	727	291
	S56	280	4.6	1680	40	355	40	80	3	355	140	9.2	355	700	0.50	2.00	0.08	0	0.309	1678	831
	S57	280	5.75	1680	40	355	40	80	3	355	140	11.5	355	700	0.50	2.00	0.08	0	0.321	2056	977
	S58	280	6.9	1680	40	355	40	80	3	355	140	13.8	355	700	0.50	2.00	0.08	0	0.326	2423	1116
	S59	280	8.05	1680	40	355	40	80	3	355	140	16.1	355	700	0.50	2.00	0.08	0	0.328	2758	1246
	S60	280	9.2	1680	40	355	40	80	3	355	140	18.4	355	700	0.50	2.00	0.08	0	0.326	3113	1371
	S61	280	4.6	1600	40	355	40	80	3	355	140	9.2	355	700	0.50	2.00	0.08	0	0.295	1678	879
	S62	280	4.6	1700	40	355	40	80	3	355	140	9.2	355	700	0.50	2.00	0.08	0	0.313	1678	821
	S63	280	4.6	1800	40	355	40	80	3	355	140	9.2	355	700	0.50	2.00	0.08	0	0.332	1678	763
	S64	280	4.6	1900	40	355	40	80	3	355	140	9.2	355	700	0.50	2.00	0.08	0	0.350	1678	719
	S65	280	4.6	1680	50	355	40	80	3	355	140	9.2	355	700	0.50	2.00	0.08	0	0.299	1678	858
	S66	280	4.6	1680	60	355	40	80	3	355	140	9.2	355	700	0.50	2.00	0.08	0	0.289	1678	883
	S67	280	4.6	1680	70	355	40	80	3	355	140	9.2	355	700	0.50	2.00	0.08	0	0.282	1678	907
	S68	280	4.6	1680	80	355	40	80	3	355	140	9.2	355	700	0.50	2.00	0.08	0	0.275	1678	930
G8	S69	280	4.6	1680	40	235	40	80	3	235	140	9.2	235	700	0.50	2.00	0.08	0	0.309	1110	599
	S70	280	4.6	1680	40	420	40	80	3	420	140	9.2	420	700	0.50	2.00	0.08	0	0.309	1985	954
	S71	280	4.6	1680	40	460	40	80	3	460	140	9.2	460	700	0.50	2.00	0.08	0	0.309	2174	1029
	S72	280	4.6	1680	40	355	50	80	3	355	140	9.2	355	700	0.50	2.00	0.08	0	0.305	1678	858
	S73	280	4.6	1680	40	355	60	80	3	355	140	9.2	355	700	0.50	2.00	0.08	0	0.302	1678	883
	S74	280	4.6	1680	40	355	70	80	3	355	140	9.2	355	700	0.50	2.00	0.08	0	0.299	1678	906
	S75	280	4.6	1680	40	355	40	60	3	355	140	9.2	355	700	0.50	2.00	0.04	0	0.311	1678	826
	S76	280	4.6	1680	40	355	40	70	3	355	140	9.2	355	700	0.50	2.00	0.06	0	0.310	1678	829
	S77	280	4.6	1680	40	355	40	90	3	355	140	9.2	355	700	0.50	2.00	0.10	0	0.309	1678	835
	S78	280	4.6	1680	40	355	40	100	3	355	140	9.2	355	700	0.50	2.00	0.12	0	0.308	1678	840
	S79	280	4.6	1680	40	355	40	80	2	355	140	9.2	355	700	0.50	2.00	0.08	0	0.310	1678	819
	S80	280	4.6	1680	40	355	40	80	4	355	140	9.2	355	700	0.50	2.00	0.07	0	0.309	1678	843
	S81	280	4.6	1680	40	355	40	80	5	355	140	9.2	355	700	0.50	2.00	0.07	0	0.308	1678	854
	S82	280	4.6	1680	40	355	40	80	3	355	140	9.2	355	700	0.50	2.00	0.08	379	0.309	1678	847
	S83	280	4.6	1680	40	355	40	80	3	355	140	9.2	355	700	0.50	2.00	0.08	759	0.309	1678	848
	S84	280	4.6	1680	40	355	40	80	3	355	140	9.2	355	700	0.50	2.00	0.08	1517	0.309	1678	823
	S85	280	4.6	1680	40	355	40	80	3	355	140	9.2	355	700	0.50	2.00	0.08	2276	0.309	1678	721
	S86	160	3.6	960	40	355	20	80	3	355	80	3.6	355	400	0.50	1.00	0.25	0	0.180	383	364
	S87	160	3.6	900	40	355	20	80	3	355	80	3.6	355	400	0.50	1.00	0.25	0	0.169	383	384
	S88	160	3.6	960	50	355	20	80	3	355	80	3.6	355	400	0.50	1.00	0.25	0	0.176	383	372
S89	160	3.6	960	60	355	20	80	3	355	80	3.6	355	400	0.50	1.00	0.25	0	0.172	383	378	
S90	160	3.6	960	70	355	20	80	3	355	80	3.6	355	400	0.50	1.00	0.25	0	0.168	383	383	
S91	160	3.6	960	80	355	20	80	3	355	80	3.6	355	400	0.50	1.00	0.25	0	0.165	383	390	
S92	160	3.6	960	40	355	25	80	3	355	80	3.6	355	400	0.50	1.00	0.25	0	0.177	383	375	
S93	160	3.6	960	40	355	30	80	3	355	80	3.6	355	400	0.50	1.00	0.25	0	0.175	383	382	
S94	160	3.6	960	40	355	35	80	3	355	80	3.6	355	400	0.50	1.00	0.25	0	0.173	383	392	
S95	160	3.6	960	40	355	20	90	3	355	80	3.6	355	400	0.50	1.00	0.32	0	0.177	383	361	
S96	160	3.6	960	40	355	20	100	3	355	80	3.6	355	400	0.50	1.00	0.41	0	0.174	383	352	
S97	160	3.6	960	40	355	20	80	2	355	80	3.6	355	400	0.50	1.00	0.26	0	0.184	383	348	
S98	160	3.6	960	40	355	20	80	4	355	80	3.6	355	400	0.50	1.00	0.24	0	0.177	383	379	

(continued on next page)

Table 2 (continued)

Group	FE model	CFDSST chord member									SHS brace member				β	τ	χ	N_c (kN)	K	N_b (kN)	N_u^{FE} (kN)
		Outer steel tube and sandwiched concrete of chord						Inner steel tube and concrete core													
		B_0 (mm)	t_0 (mm)	L_0 (mm)	f_{c0} (MPa)	f_{y0} (MPa)	h_s (mm)	B_2 (mm)	t_2 (mm)	f_{y2} (MPa)	B_1 (mm)	t_1 (mm)	f_{y1} (MPa)	L_1 (mm)							
	S99	160	3.6	960	40	355	20	80	5	355	80	3.6	355	400	0.50	1.00	0.23	0	0.174	383	392
	S100	160	3.6	960	40	355	20	80	3	355	80	3.4	355	400	0.50	0.94	0.25	0	0.171	363	359
	S101	160	3.6	960	40	355	20	80	3	355	80	3.2	355	400	0.50	0.89	0.25	0	0.163	342	350
	S102	160	3.6	960	40	355	20	80	3	355	80	3.0	355	400	0.50	0.93	0.25	0	0.154	322	336
	S103	180	3.8	1080	40	355	30	80	3	355	90	3.8	355	450	0.50	1.00	0.20	0	0.177	456	438
	S104	180	3.8	1000	40	355	30	80	3	355	90	3.8	355	450	0.50	1.00	0.20	0	0.164	456	468
	S105	180	3.8	1080	50	355	30	80	3	355	90	3.8	355	450	0.50	1.00	0.20	0	0.172	456	448
	S106	180	3.8	1080	60	355	30	80	3	355	90	3.8	355	450	0.50	1.00	0.20	0	0.168	456	457
	S107	180	3.8	1080	70	355	30	80	3	355	90	3.8	355	450	0.50	1.00	0.20	0	0.164	456	464
	S108	180	3.8	1080	80	355	30	80	3	355	90	3.8	355	450	0.50	1.00	0.20	0	0.161	456	471
	S109	180	3.8	1080	40	355	35	80	3	355	90	3.8	355	450	0.50	1.00	0.20	0	0.175	456	450
	S110	180	3.8	1080	40	355	40	80	3	355	90	3.8	355	450	0.50	1.00	0.20	0	0.173	456	460
	S111	180	3.8	1080	40	355	45	80	3	355	90	3.8	355	450	0.50	1.00	0.20	0	0.172	456	469
	S112	180	3.8	1080	40	355	30	60	3	355	90	3.8	355	450	0.50	1.00	0.10	0	0.180	456	430
	S113	180	3.8	1080	40	355	30	70	3	355	90	3.8	355	450	0.50	1.00	0.15	0	0.178	456	435
	S114	180	3.8	1080	40	355	30	90	3	355	90	3.8	355	450	0.50	1.00	0.25	0	0.175	456	442
	S115	180	3.8	1080	40	355	30	100	3	355	90	3.8	355	450	0.50	1.00	0.32	0	0.173	456	443
	S116	180	3.8	1080	40	355	30	80	2	355	90	3.8	355	450	0.50	1.00	0.20	0	0.179	456	423
	S117	180	3.8	1080	40	355	30	80	4	355	90	3.8	355	450	0.50	1.00	0.19	0	0.175	456	451
	S118	180	3.8	1080	40	355	30	80	5	355	90	3.8	355	450	0.50	1.00	0.18	0	0.173	456	462
	S119	180	3.8	1080	40	355	30	80	3	355	90	3.6	355	450	0.50	0.95	0.20	0	0.169	432	434
	S120	180	3.8	1080	40	355	30	80	3	355	90	3.4	355	450	0.50	0.89	0.20	0	0.160	409	424
	S121	180	3.8	1080	40	355	30	80	3	355	90	3.2	355	450	0.50	0.84	0.20	0	0.152	386	406
	S122	280	4.6	1680	40	355	40	80	3	355	140	4.6	355	700	0.50	1.00	0.08	0	0.171	868	814
	S123	280	4.6	1600	40	355	40	80	3	355	140	4.6	355	700	0.50	1.00	0.08	0	0.163	868	851
	S124	280	4.6	1680	50	355	40	80	3	355	140	4.6	355	700	0.50	1.00	0.08	0	0.165	868	836
	S125	280	4.6	1680	60	355	40	80	3	355	140	4.6	355	700	0.50	1.00	0.08	0	0.160	868	860
	S126	280	4.6	1680	70	355	40	80	3	355	140	4.6	355	700	0.50	1.00	0.08	0	0.156	868	882
	S127	280	4.6	1680	80	355	40	80	3	355	140	4.6	355	700	0.50	1.00	0.08	0	0.152	868	902
	S128	280	4.6	1680	40	355	50	80	3	355	140	4.6	355	700	0.50	1.00	0.08	0	0.169	868	837
	S129	280	4.6	1680	40	355	60	80	3	355	140	4.6	355	700	0.50	1.00	0.08	0	0.167	868	857
	S130	280	4.6	1680	40	355	70	80	3	355	140	4.6	355	700	0.50	1.00	0.08	0	0.165	868	874
	S131	280	4.6	1680	40	355	40	80	3	355	140	4.4	355	700	0.50	0.95	0.08	0	0.164	830	808
	S132	280	4.6	1680	40	355	40	80	3	355	140	4.2	355	700	0.50	0.91	0.08	0	0.157	793	799
	S133	280	4.6	1680	40	355	40	80	3	355	140	4.0	355	700	0.50	0.87	0.08	0	0.151	757	781

Table 3
Coefficients α_1 , α_2 , and α_3 [28].

Cross-section Type	$\bar{\lambda}$ condition	α_1	α_2	α_3
a	-	0.41	0.986	0.152
b	-	0.65	0.965	0.300
c	$\bar{\lambda} \leq 1.05$	0.73	0.906	0.595
	$\bar{\lambda} > 1.05$		1.216	0.302
d	$\bar{\lambda} \leq 1.05$	1.35	0.868	0.915
	$\bar{\lambda} > 1.05$		1.375	0.432

concrete-filled steel tubes (CFST) in bending is that the curve tends to flatten in the later phases of loading [34]. As seen in Table 4(d), the ultimate load N_u^{FE} typically corresponds to a mid-span deflection of $L_0/50$.

4.3. Load-strain response

Herein, the load-strain diagrams of T-joints with different K values are compared in order to further assess the behaviour of T-joints with various failure modes, as shown in Fig. 11. The T-joints considered are S102 ($K=0.154$), S88 ($K=0.176$), S97 ($K=0.184$) and S1 ($K=0.203$). In the figure, strain is given in the horizontal axis, and the load applied to the brace is in the vertical axis. The longitudinal strains are measured at: (i) the brace steel tube midpoint, (ii) the compressive side at the top of the cross-section in the chord mid-span, and (iii) the tensile side at the bottom of the cross-section in the chord mid-span. Tensile strains are shown as positive values in the diagrams, whereas compressive strains are shown as negative values.

From Fig. 11, it is evident that all specimens experience yielding in the chords before the brace. The primary distinction is that the brace strains in T-joints S102 and S88 (with $K < 0.18$) eventually reach yielding, whereas those in T-joint models S97 and S1 (with $K \geq 0.18$) do not. When the T-joint reaches its maximal load ($N_u^{FE}=336$ kN and 372 kN for S102 and S88, respectively), the strain in the brace reaches the yield strain ($1690\mu\epsilon$) for S102 and S88 as seen in Fig. 11(a) and (b), respectively. This suggests that the brace is the primary factor influencing the T-joint bearing capability. The load drops as soon as the brace yields, but the strain inside the brace keeps rising because of severe local buckling

failure. This buckling lessens the chord bending and occasionally even causes a small recovery in deformation. As a result of brace failure, the chord tensile and compressive strains diminish.

On the other hand, as examined in Section 4.1, T-joints S97 and S1, with $K \geq 0.18$, exhibit significant chord bending deformation without brace buckling. Fig. 11(c) and (d) show that the brace strain falls short of the yield level. The chord experiences substantial bending deformation, which results in greater strains at the ultimate load capacity (N_u^{FE}). The strain in the chord at failure increases with the K value.

4.4. Influence of key parameters

This section examines the influence of key parameters on the overall response of the T-joints. Each parameter is considered in isolation in order to determine their effect directly.

4.4.1. Chord cross-section configuration

Herein, a comparison is made between the effect of different chord cross-section configurations on the ultimate load N_u^{FE} and the strength-to-weight (S/W_T) ratio of the T-joints, the latter of which has not been considered elsewhere. FE Models S1, S6, and S46 were used as a reference, and other T-joints with hollow steel stiffened tube (HSST), CFSST and CFDT chords were generated. These cross-sections are provided in Table 5, where W_C and W_T are the weight of the chord and the T-joint, respectively. The weight calculations of the joints were based on the cubic meter self-weights of plain concrete and steel, which were taken as 2400 kg/m^3 and 7850 kg/m^3 , respectively. The load-displacement curves of the T-joints with different chord configurations are presented in Fig. 12, where it is shown that they all exhibit similar load-displacement responses.

The analysis illustrates that using concrete are/or inner steel tubes affects the value of N_u^{FE} of the T-joint, but the differences do not exceed 10 %, except for the ‘‘Hollow steel stiffened tube’’ chord configuration, whose ultimate load is less than half of the CFDSST T-joint load. This is because the T-joint failed by web crippling of the chord tubular section under the concentrated transverse force of the brace in the latter configuration [35], as shown in Fig. 13. This mode is defined as the interior-one-flange (IOF) web crippling load condition according to the North American Specification NAS [36], which requires attention in

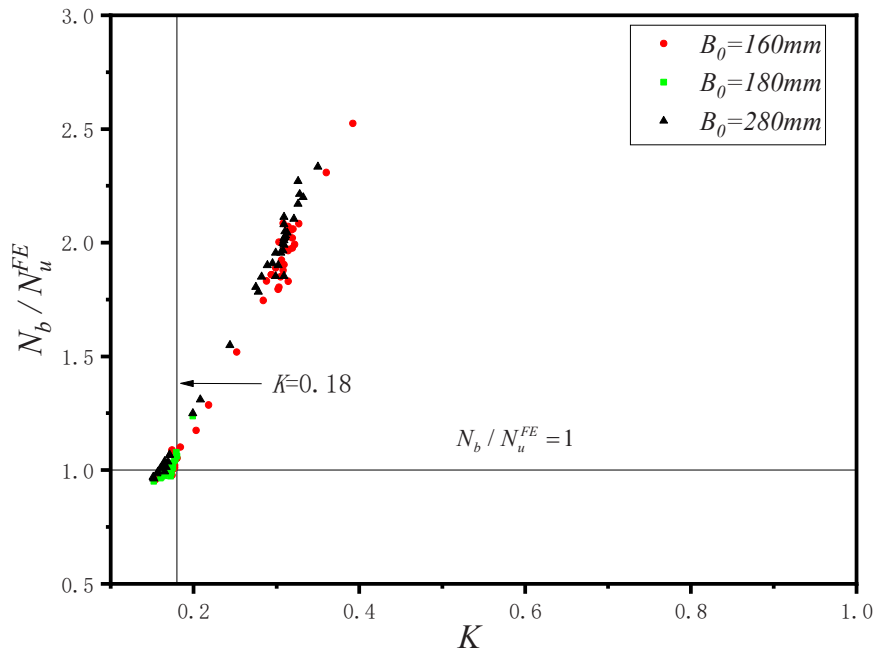
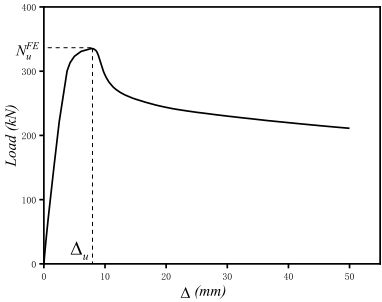
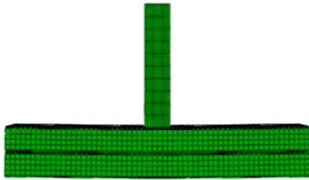
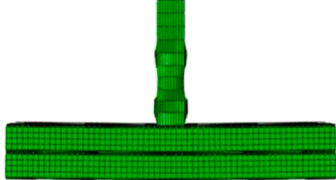
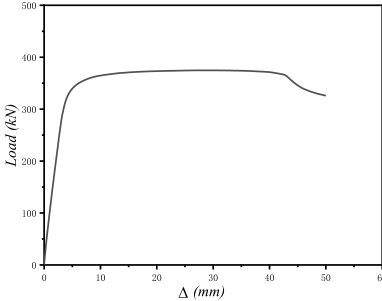
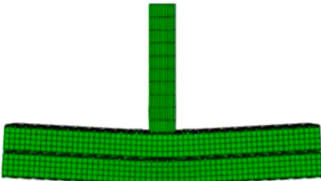
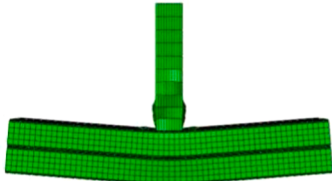
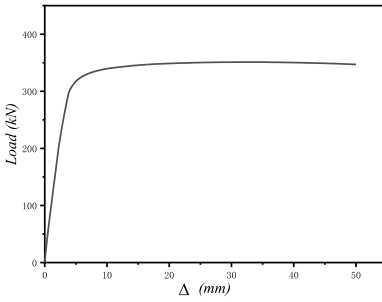
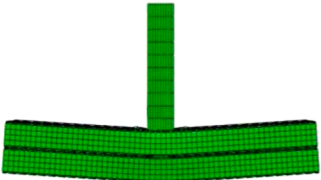
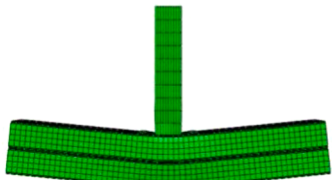
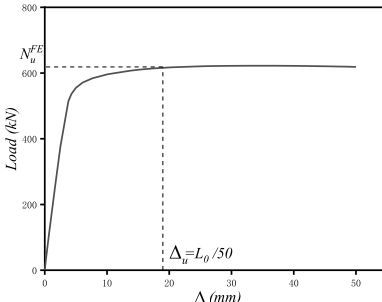
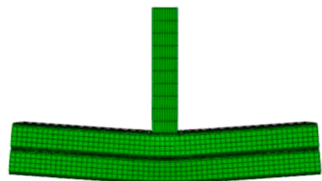
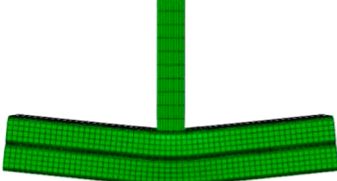


Fig. 10. Relationship between K and N_b/N_u^{FE} .

Table 4
Overall load-deflection (N - Δ) responses and failure modes of the T-joint specimens.

N - Δ response	Deformation at ultimate load	Final deformation
(a) S102 ($K=0.154$)		
		
(b) S88 ($K=0.176$)		
		
(c) S97 ($K=0.184$)		
		
(d) S1 ($K=0.203$)		
		

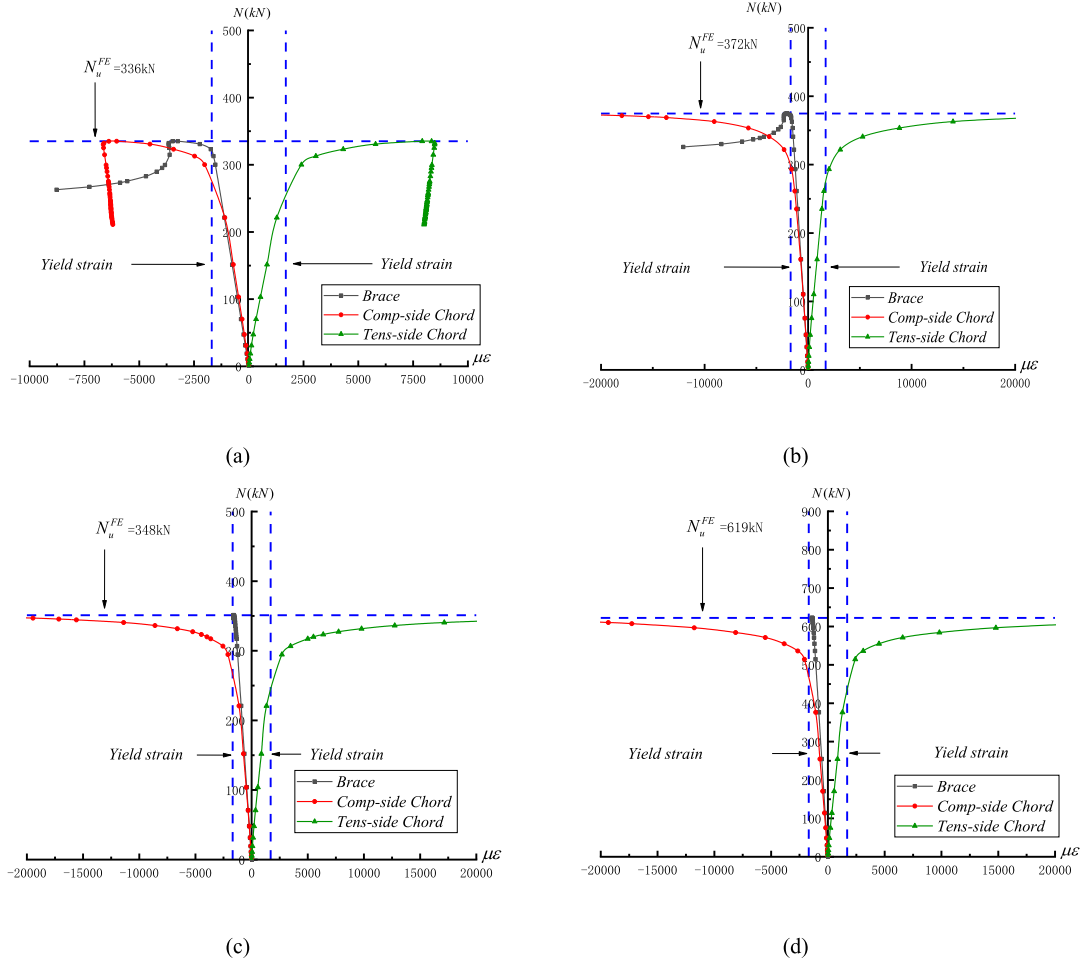



Fig. 11. Load-strain curves of T-joints with different K values for: (a) S102 ($K = -0.154$), (b) S88 ($K = -0.176$), (c) S97 ($K = -0.184$) and (d) S1 ($K = -0.203$).

Table 5

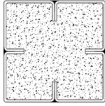
Comparisons between T-joints with different chord configurations.

Specimens	Chord type	f_{co} (MPa)	f_{yo} (MPa)	B_2 (mm)	t_2 (mm)	f_{y2} (MPa)	W_C	W_T	N_u^{FE} (kN)	S/W_T
$B_0 = 160$ mm, $t_0 = 7.2$ mm, $L_0 = 960$ mm, $f_{y0} = 355$ MPa										
S1-1	HSST	-	355	-	-	-	398	469	289	0.62
S1-2	CFSST	40	355	-	-	-	860	931	608	0.65
S1	CFDSST	40	355	80	3	355	782	853	619	0.73
S1-3	CFDT	40	355	80	3	355	905	976	658	0.67
$B_0 = 180$ mm, $t_0 = 7.2$ mm, $L_0 = 1080$ mm, $f_{y0} = 355$ MPa										
S6-1	HSST	-	355	-	-	-	482	577	332	0.58
S6-2	CFSST	40	355	-	-	-	1137	1232	676	0.55
S6	CFDSST	40	355	80	3	355	1047	1142	704	0.62
S6-3	CFDT	40	355	80	3	355	1186	1281	723	0.56
$B_0 = 280$ mm, $t_0 = 4.6$ mm, $L_0 = 1680$ mm, $f_{y0} = 355$ MPa										
S46-1	HSST	-	355	-	-	-	782	1060	171	0.16
S46-2	CFSST	40	355	-	-	-	3630	3908	795	0.20
S46	CFDSST	40	355	80	3	355	3491	3768	831	0.22
S46-3	CFDT	40	355	80	3	355	3706	3984	839	0.21

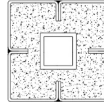
KEY:



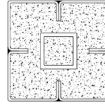
HSST



CFSST



CFDSST



CFDT

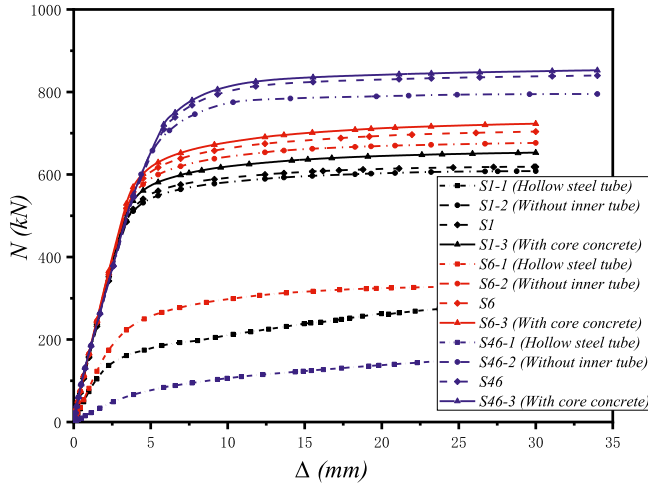


Fig. 12. The load-displacement curves of the T-joints with different chord configurations.

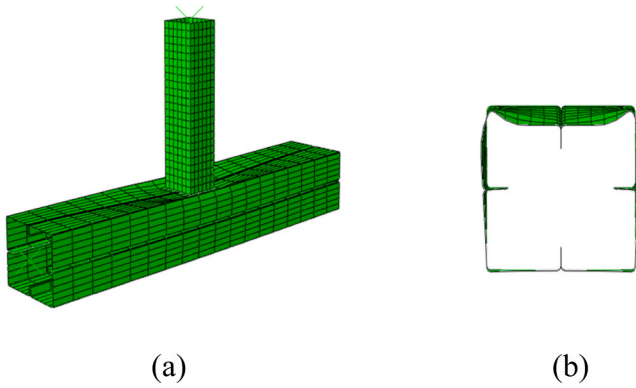
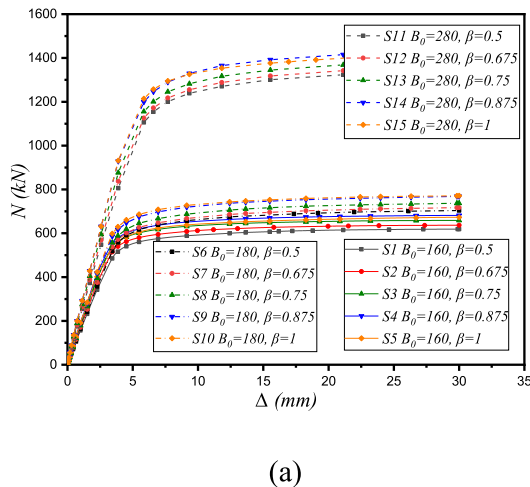


Fig. 13. Failure mode of T-joint with hollow steel stiffened tubular chord (S1-1): (a) isometric view and (b) cross-section of chord at mid-span.

future research. In contrast, all other T-joints failed by flexure of the steel-concrete composite chords. Hence, this highlights the importance of utilising a steel-concrete composite chord in T-joints. As indicated in Table 5, the CFDT-to-SHS T-joint exhibits the highest load carrying capacity compared with other composite chord configurations. However, choosing the most effective composite chord configuration would be



related to the S/W_T ratios of the different T-joints, which indicates that the CFDSST-to-SHS T-joint provides the highest ratio, and in turn represents the most efficient solution.

4.4.2. Brace-to-chord width ratio (β)

In this section, the FE data from three different groups: G1 (S1-S5), G2 (S6-S10), and G3 (S11-S15) is evaluated in order to determine the effect of the brace-to-chord width ratio β (where $\beta = B_1/B_0$) on the behaviour and ultimate bearing capacity of CFDSST-to-SHS T-joints. Fig. 14(a) depicts the load-displacement curves for various B_0 values in relation to changes in β , while Fig. 14(b) displays the relationship between the ultimate bearing capacity of the T-joint (N_u^{FE}) and β for three groups of joints with different β values. As noted, N_u^{FE} stands for the ultimate bearing capacity, and $L_0/50$, as established in Section 3.2, is the corresponding displacement Δ . The data clearly show that N_u^{FE} becomes higher as β increases. For a B_0 value of 160 mm, N_u^{FE} increases by 8.7 %, from 619 kN to 673 kN, as β increases from 0.5 to 1. Similarly, N_u^{FE} increases by 9.5 % and 6.0 %, respectively, when B_0 is 180 mm and 280 mm. Nevertheless, for all the cross-sections considered herein, N_u^{FE} reduces quite marginally when β rises from 0.875 to 1.0, as indicated in Fig. 14(b). The chord and brace are the same width at $\beta = 1.0$. As shown in Fig. 15, the chord steel tube cross-section corners have a cold-formed bending angle, leaving two non-contact sections at the brace-to-chord intersection location, hence β is, in effect, less than unity. Moreover, the brace load is transmitted through two edges only, and therefore concentrated over a smaller area. As a result, the brace cross-section experiences an uneven force distribution, which eventually lowers the T-joint bearing capacity.

4.4.3. Brace-to-chord thickness ratio (τ)

The results from three distinct cross-sections are examined in order to assess the influence of the brace-to-chord thickness ratio (τ) on the ultimate load of CFDSST-to-SHS T-joints. This ratio is determined as

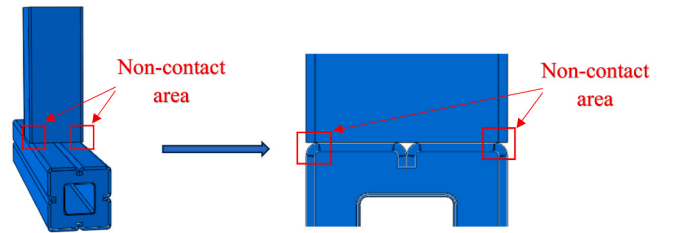


Fig. 15. Schematic of the non-contact area ($\beta=1$).

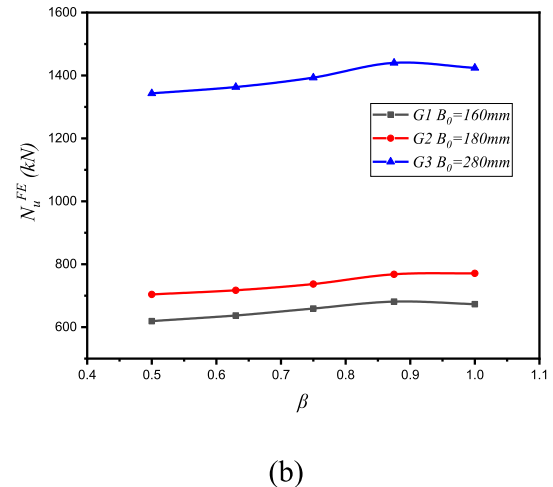


Fig. 14. Influence of β on the behaviour of CFDSST-to-SHS T-joints including: (a) load-displacement responses and (b) effect on N_u^{FE} .

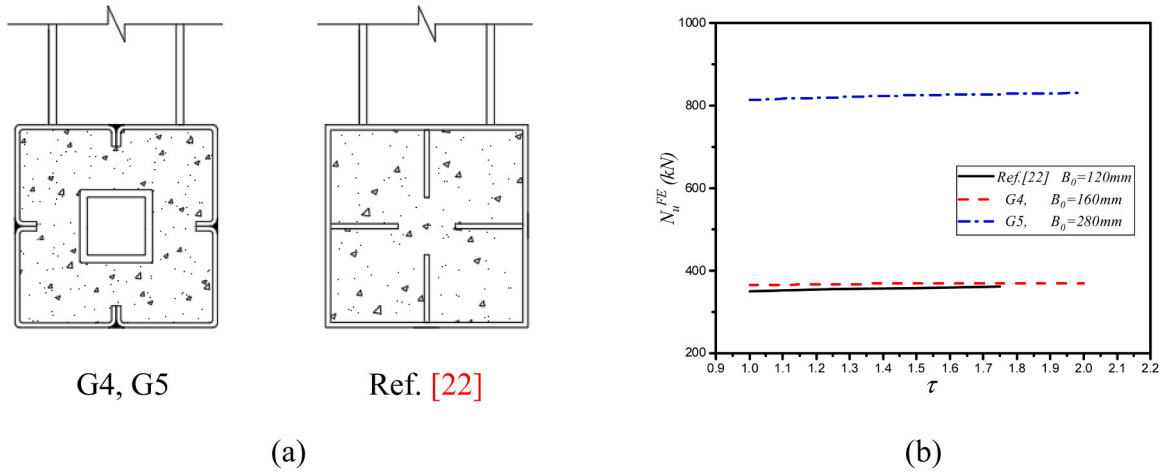


Fig. 16. Effect of τ on N_u^{FE} for different cross-sections including: (a) G4, G5 and Ref. [22] and (b) parametric study results.

$\tau = t_1/t_0$, where t_1 and t_0 are the brace and chord thicknesses, respectively.

Referring to Table 2, these cross-sections are depicted in Fig. 16(a) and consist of specimens from Ref. [22], with $B_0 = 120$ mm, as well as G4 (S16-S20), with $B_0 = 160$ mm, and G5 (S21-S25), with $B_0 = 280$ mm. The relationship between τ and the ultimate bearing capacity N_u^{FE} for the three T-joint groups is shown in Fig. 16(b). Notably, the chord types vary: the specimens from Ref. [22] are made up of regular CFST with longitudinal stiffeners, whereas G4 and G5 are CFDSST members. N_u^{FE} increases from 364 kN to 369 kN for Group G4, where $B_0 = 160$ mm, as τ increases from 1.0 to 2.0, signifying a 1.37 % increase in capacity. Likewise, for Group G5 with $B_0 = 280$ mm, τ rises from 1.0 to 2.0, causing N_u^{FE} to increase by 2.1 %, from 814 kN to 831 kN. With $B_0 = 120$ mm, τ increases from 1.0 to 1.75 for the specimens from Ref. [22], and N_u^{FE} increases from 350 kN to 361 kN, indicating a 3.1 % capacity enhancement. These findings clearly show that the influence of τ on the final load N_u^{FE} is relatively limited. This effect seems to hold true for chords of varying cross-sectional diameters.

4.4.4. Concrete strength

Ten T-joints with different sandwiched concrete strengths (f_{c0}) ranging from 40 MPa to 80 MPa were performed in order to investigate the effect of concrete strength on the performance of CFDSST-to-SHS T-joints; T-joints S46 and S55-S58 with $B_0 = 280$ mm and T-joints S26 and S35-S38 with $B_0 = 160$ mm. The influence of concrete strength on the load of CFDSST-to-SHS T-joint is assessed in terms of: (a) load-

displacement responses and (b) influence of concrete strength on N_u^{FE} as illustrated in Fig. 17. As can be noticed, the ultimate load-bearing capacity of the CFDSST-to-SHS T-joint model increases when the strength of the sandwiched concrete increases. As the strength of the sandwiched concrete increased, the ultimate bearing capacity N_u^{FE} for T-joints with $B_0 = 280$ mm improved by 11.9 %, from 831 kN to 930 kN. Likewise, N_u^{FE} increased by 7.3 % from 370 kN to 397 kN for T-joints with $B_0 = 160$ mm. As expected, given the increased volume of concrete, these results show that joints with larger cross-sectional dimensions are more significantly affected by the increase in the value of f_{c0} .

4.4.5. Steel grade

Four specimens with different steel strengths ($f_y = 235$ MPa, 355 MPa, 420 MPa, and 460 MPa) were designed for two distinct cross-sections ($B_0 = 160$ mm and 280 mm) in order to investigate the influence of steel strength on the performance of CFDSST-to-SHS T-joints, as seen in Table 2. The load-displacement curves for various B_0 values in relation to variations in steel strength are shown in Fig. 18(a), while the relationship of N_u^{FE} vs f_y are presented in Fig. 18(b). The results show that as the steel strength increases, so does the CFDSST-to-SHS T-joint ultimate load-bearing capacity. As the steel strength increased from 235 MPa to 460 MPa, the ultimate bearing capacity (N_u^{FE}) for $B_0 = 160$ mm increased from 265 kN to 456 kN. Over the same range of steel strengths, the ultimate bearing capacity for $B_0 = 280$ mm increased from 599 kN to 1029 kN. When the steel yield strength increased from 235 MPa to 355 MPa, 420 MPa, and 460 MPa, N_u^{FE} increased by 40 %, 40 %, and 40 %, respectively.

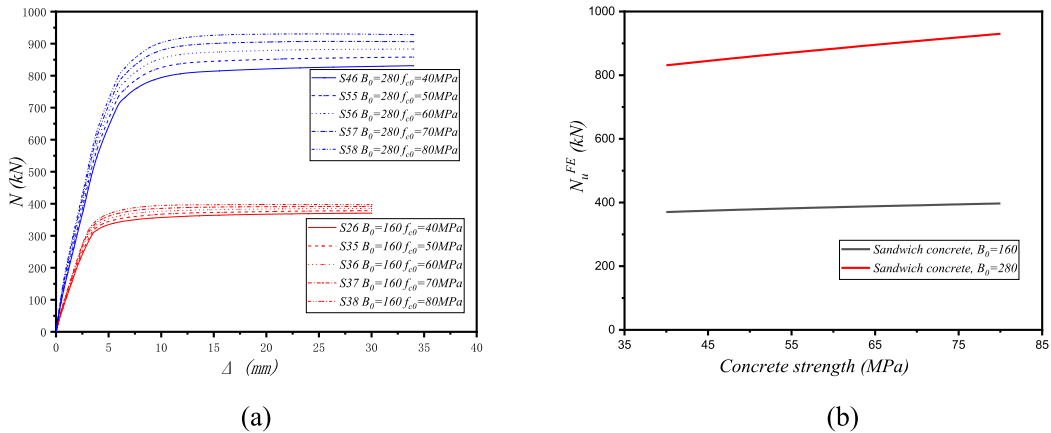


Fig. 17. Influence of concrete strength on the capacity of CFDSST-to-SHS T-joint including: (a) load-displacement response and (b) influence of concrete strength on N_u^{FE} .

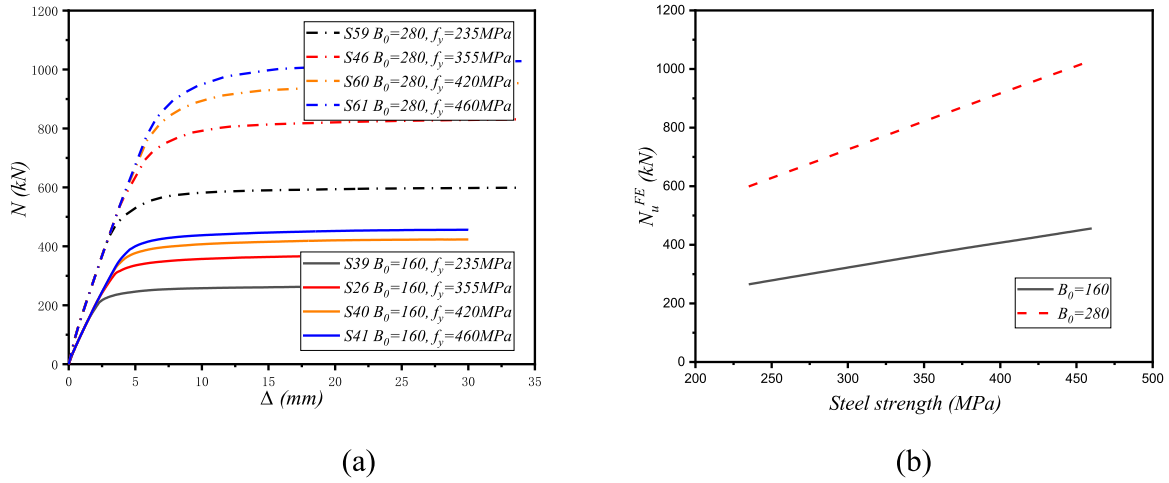


Fig. 18. Influence of steel grade on: (a) load-displacement response of different sections and (b) ultimate capacity N_u^{FE} .

60 %, and 72 %, respectively, for T-joints with $B_0=160$ mm. For T-joints with $B_0=280$ mm, the corresponding increases were 39 %, 59 %, and 72 %, respectively. The significance of steel characteristics on the response of CFDSST-to-SHS T-joints is highlighted by these results, which clearly show that the steel strength influences the ultimate bearing capacity more than the concrete strength, although the presence of concrete is vital in terms of preventing or delaying local buckling.

4.4.6. Axial load in the chord

The application of axial force causes a significant change in the mechanical behaviour of concrete-filled steel tube (CFST) structures. Therefore, several axial forces were applied to the chord in the FE model in order to investigate the influence of the chord axial load on the performance of CFDSST-to-SHS T-joints. The load-displacement curves for the axial force magnitudes, which were determined to be 0.0, 0.1, 0.2, 0.4, and 0.6 times the CFDSST chord ultimate axial load-carrying capacity ($N_{c,ul}$), are plotted in Fig. 19(a) for comparison, while Fig. 19(b) shows the relationship between the ultimate strength N_u^{FE} and the axial load ratio of the chord ($N_c/N_{c,ul}$ ratios). The results of the axial load applied to the chord (N_c) for Models S46, S62-S65, S26, and S42-S45 are given in Table 2, while $N_{c,ul}$ is determined as follows [31]:

$$N_{c,ul} = (A_{sy,eff} + A_{cs}) \left(1.18 + 0.85 \xi_{so} \right) f_{ck,s} + (A_{si} + A_{cc}) \left(1.18 + 0.85 \xi_{si} \right) f_{ck,i} + A_{ss} f_{ys} \quad (14)$$

where $f_{ck,i}$ and $f_{ck,s}$ are the compressive strengths of the core and sandwiched concrete, respectively; $A_{sy,eff}$, A_{cs} , A_{si} , A_{cc} and A_{ss} are effective cross-sectional area of the outer steel tube, sandwiched concrete area, inner steel tube area, core concrete area and stiffeners area, respectively; and ξ_{so} and ξ_{si} are confinement factors of outer steel tube and inner steel tube, respectively [31]. It is clear from Fig. 19 that the load-displacement behaviour of the T-joints is influenced by the axial load in the chord. The ultimate load-carrying capacity of the joint declines with increasing axial load, hence affecting the overall stiffness. This behaviour is in line with findings in other CFST structures, which show that the chord resistance to bending and shear forces decreases with increasing axial load. The relationship between the axial force and joint strength hence needs to be explicitly accounted for in design procedures.

Fig. 19 illustrates two key features with respect to the influence of the axial load on CFDSST-to-SHS T-joints. First, as the axial load applied to the chord increases, the ultimate load N_u^{FE} clearly changes and progressively decreases. When $B_0=160$ mm, the ultimate load drops from 370 kN to 291 kN. Likewise, N_u^{FE} decreases from 831 kN to 721 kN for $B_0=280$ mm. It should be mentioned, though, that when the axial load acting on the chord is less than 0.2 times the ultimate axial load-carrying capacity $N_{c,ul}$, the reduction in ultimate load is only slight. This suggests that the T-joint retains a significant amount of its load-bearing capacity at lower axial loads. The second feature is the phase of plastic behaviour, with the load-displacement curves exhibiting a more noticeable

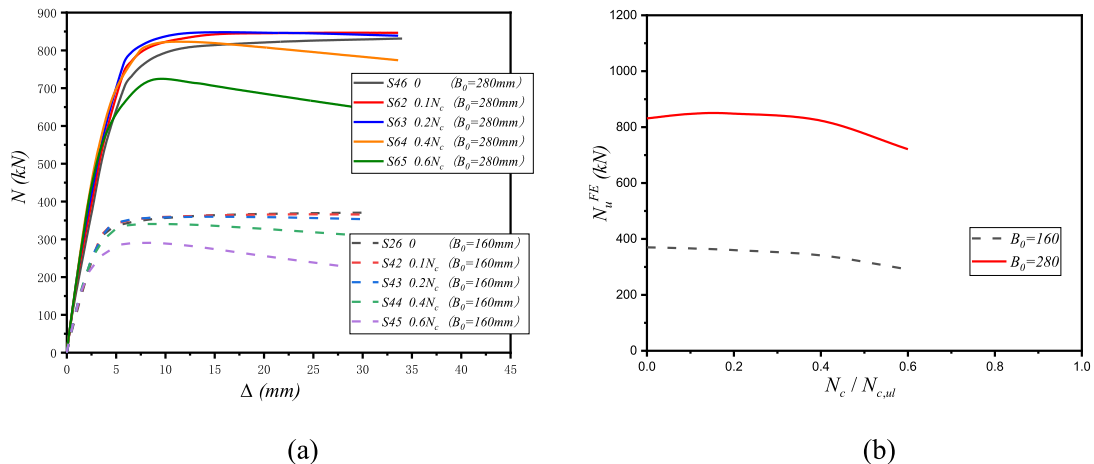


Fig. 19. Influence of N_c on: (a) load-displacement responses and (b) ultimate strength N_u^{FE} .

downward trend as the axial load applied to the chord increases from 0.0 to $0.6N_{c,ul}$. This implies that the degradation in load-carrying capacity during the plastic phase is more pronounced with higher the axial load on the chord. This behaviour suggests that the joint undergoes a more rapid decline in performance after reaching the ultimate load because it enters the plastic phase earlier and experiences more significant stiffness degradation under higher axial loads. These findings indicate that although the axial load does affect the ultimate load capacity, its effects are most noticeable during the plastic phase, where the performance declines more sharply as the axial forces increases.

The load-strain responses for CFDSST-to-SHS T-joint configurations with varying axial loads on the chord members are shown in Fig. 20. The chord upper and lower sides first show compressive strain at low applied axial load N_c levels. The compressive strains increase with increasing N_c . T-joints S45 and S65 exhibit the highest axial loads at $0.6N_{c,ul}$. As a result, the specimens are already experiencing considerable compressive strain before any bending deformation from the brace load takes place, noting that their load-strain curves begin on the leftmost side of the horizontal axis.

The axial force applied to the brace causes bending deformation in the chord, resulting in tensile strain on the chord lower side and compressive strain on its upper side. The initial compressive strain brought on by the axial load is superimposed on top of these strains. As a result, the tensile side (lower side) gradually transitions from compressive to tensile strain, while the upper side reaches yield earlier due to the accumulation of superimposed compressive strains. Because of the combined effects of axial load and bending deformation, the upper side strain for T-joints with high axial force in the chord (such as S45 and S65) enters the yield stage earlier. Compared to joints with lower or no axial load, these joints exhibit a quicker progression towards yielding and, as a result, have lower load-bearing capacities. When higher axial loads are applied, this early yielding results in lower joint ultimate load-carrying capacity. In conclusion, the axial load in the chord has a major influence on the strain behaviour, instigating the compressive side yielding and lowering the T-joint overall load-bearing capacity. The closer the axial load gets to $0.6N_{c,ul}$, the more severe this effect becomes.

4.4.7. Stiffener width

The stiffeners in CFDSST chords are usually made by rolling the steel edges. This can improve the composite action by increasing the contact area between the concrete and the steel tube, strengthening the bond between the two materials, and reducing the relative slip. However, the minimum width $h_{s,min}$ of the stiffeners for CFDSST chords should comply with Eq. 15 [29]:

$$h_{s,min} = \sqrt[3]{\frac{12I_s}{2t_0}} \text{ and } I_s = 3.1 \times 10^{-4} \left(\frac{0.5B_0 - 2t_0}{t_0} \right)^{3.5} \frac{f_{y0}}{280} t_0^4 \quad (15)$$

Herein, eight distinct stiffener widths (h_s) and two cross-section sizes ($B_0=160$ mm, 280 mm) were investigated, as shown in Fig. 23. Note that the minimum $h_{s,min}$ values are 18 mm and 39 mm for T-joint cases of $B_0=160$ mm and $B_0=280$ mm, respectively, in accordance with Eq. 23. Therefore, h_s values ranged from 20 to 35 mm for T-joints with $B_0=160$ mm, and from 40 to 70 mm for T-joints with $B_0=280$ mm. The figure illustrates the influence of different stiffener widths on: (a) load-displacement responses and (b) ultimate strength N_u^{FE} . It is observed that the ultimate capacity N_u^{FE} increases for relatively higher h_s values. Arrangements with $B_0=160$ mm and $h_s=20$ mm or 35 mm result in a 9.5 % increase in N_u^{FE} from 370 kN to 405 kN. When $B_0=280$ mm and $h_s=40$ mm or 70 mm, the corresponding values are 831 kN and 906 kN, respectively (9.0 % increase). Based on these results, it is determined that increasing h_s may be beneficial in enhancing the capacity of the CFDSST-to-SHS T-joints.

4.4.8. Size of the inner steel tube

To explore the influence of varying inner steel tube dimensions on the ultimate load N_u^{FE} , two groups of specimens with different inner steel tube widths (B_2) and thicknesses (t_2) were designed, with widths ranging from 60, 70, 80, 90 and 100 mm and thicknesses of 2, 3, 4 and 5 mm, respectively. As shown in Fig. 22, for specimens with $B_0=160$ mm, as the inner steel tube width increased from 60 mm to 80 mm, the ultimate bearing capacity N_u^{FE} rose from 365 kN to 370 kN (1.4 % increase); however, when the width further increased from 80 mm to 100 mm, N_u^{FE} reduced from 370 kN to 363 kN (1.9 % decrease). For case of T-joints with $B_0=280$ mm, as the inner steel tube width increased from 60 mm to 100 mm, N_u^{FE} increased from 826 kN to 840 kN (1.7 % improvement). For arrangements with $B_0=160$ mm, as the inner steel tube thickness increased from 2 mm to 5 mm, N_u^{FE} increased from 353 kN to 403 kN (14.2 % increase). When the chord width was $B_0=280$ mm, N_u^{FE} increased from 819 kN to 854 kN (4.3 % improvement) for a greater steel tube thickness. In addition, increasing B_2 and t_2 did not affect the failure modes; the brace did not fail before the T-joints reaching their maximum load-bearing capacity, consistently exhibiting the same failure mode.

5. Design predictions for joint capacity

In accordance with the failure modes and the criteria discussed in Section 4.2, the load bearing capacity of CFDSST-to-SHS T-joints is

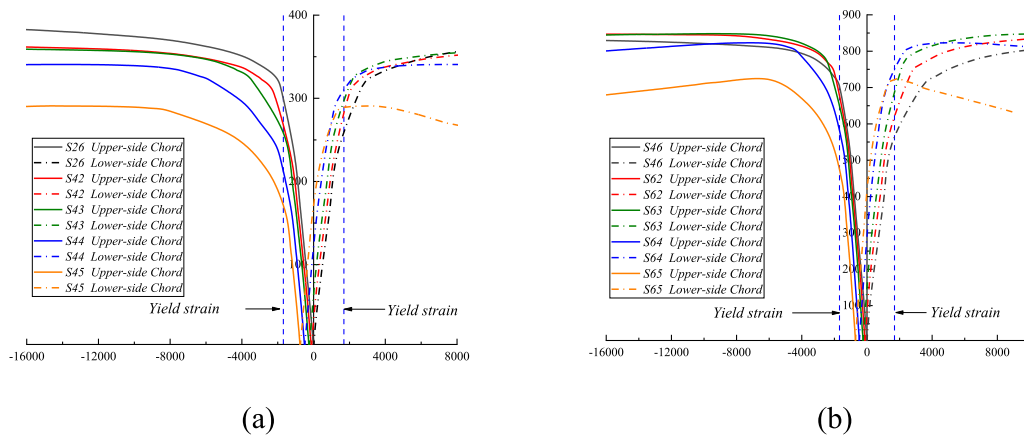


Fig. 20. Load-strain curves of T-joints with different axial load on the chord including arrangements with B_0 of: (a) 160 mm and (b) 280 mm.

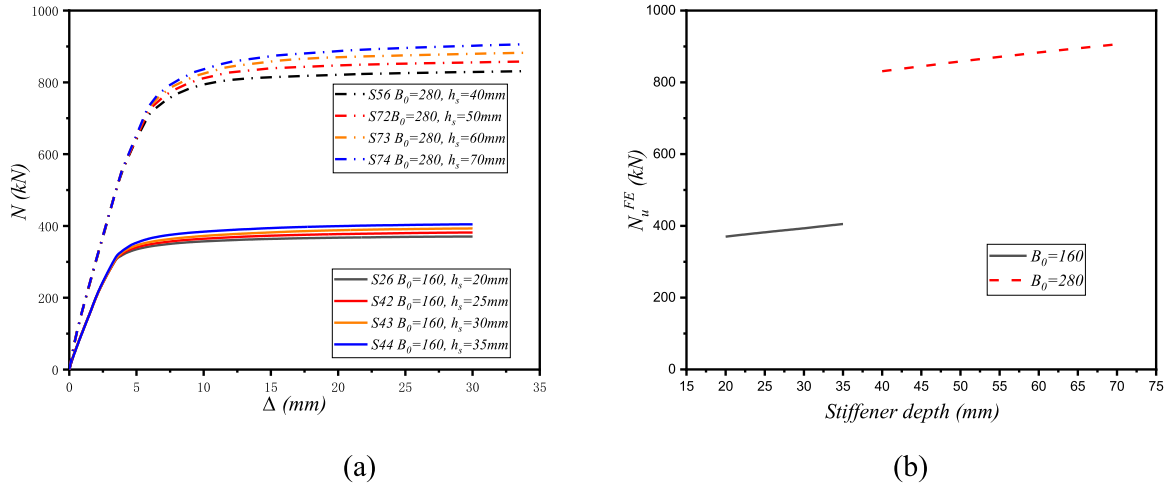


Fig. 21. Influence of different stiffener widths on: (a) load-displacement responses and (b) ultimate strength N_u^FE .

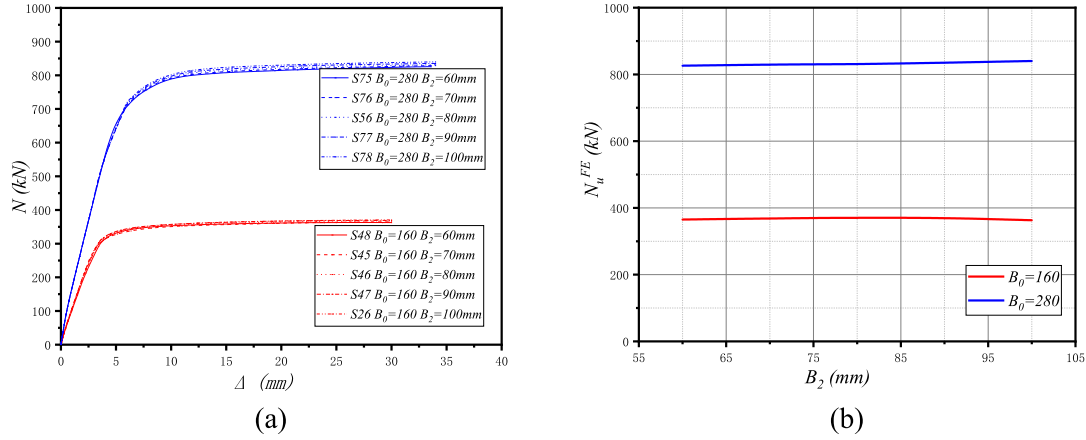


Fig. 22. The influence of width of inner steel tube on (a) load versus displacement and (b) the ultimate strength N_u^FE .

governed by two cases: (i) brace-dominated failure ($K < 0.18$), where the capacity is predicted by the brace compression resistance, N_b , according to Eq. 9, and (ii) chord-dominated failure ($K \geq 0.18$), where the resistance is based on the chord flexural capacity. For the latter, established design procedures and guidelines, such as those from DBJ/T13-51 [33], AIJ [37], AISC-LRFD [38], EC4 [39] and BS-ISO [40] are used to determine the flexural bearing capacity of the CFDSST chord. These approaches differ in terms of assumptions regarding material characteristics, steel-concrete interaction, and failure mechanisms considered, as discussed below. The flexural capacities for CFDSST chords based on these various approaches are shown in Table 6.

Table 6
Comparison of capacity between design methods and FE results.

Statistical parameters	DBJ [33]	AIJ [37]	AISC [38] /EC4 [39]	BS [40]	Limit balance theory [22]
	$\frac{M_{u,DBJ}}{M_u^{FE}}$	$\frac{M_{u,AIJ}}{M_u^{FE}}$	$\frac{M_{u,AISC}}{M_u^{FE}}$	$\frac{M_{u,BS}}{M_u^{FE}}$	$\frac{M_{u,LBT}}{M_u^{FE}}$
Mean	0.73	0.92	1.11	0.89	0.95
SD	0.034	0.058	0.060	0.098	0.041
Max	0.86	1.08	1.42	1.16	1.22
Min	0.67	0.77	0.83	0.75	0.86

5.1. DBJ/T13-51

The method for determining the bending capacity of a square CFST according to DBJ/T13-51 [33] is given by Eq. 16:

$$M_{u,DBJ} = \gamma_m W_{sc} f_{sc} + W_s (f_s - f_{sc}) \quad (16)$$

where γ_m represents the section bending plastic development coefficient, which is determined by the confinement coefficient (θ_{sc}). The values of γ_m and θ_{sc} are calculated using Eq. 17 and Eq. 18, respectively:

$$\gamma_m = 1.04 + 0.48 \ln(\theta_{sc} + 0.1) \quad (17)$$

$$\theta_{sc} = A_s f_y / A_c f_{ck} \quad (18)$$

In these equations, f_y and f_{ck} denote the material strengths of the steel tube and the concrete infill, respectively. W_{sc} is the section bending modulus within the plane of bending, while W_s refers to the section modulus of stiffeners, which is described by Eq. 19:

$$W_s = n_s t_s h_s (D - 2t - h_s) \quad (19)$$

In the equation, f_{sc} and f_s are section combined bending strength and stiffener strength, respectively. In addition, h_s , t_s and n_s represent the width, thickness, and number of stiffeners, respectively, while D and t are the width and thickness of the square steel tube.

5.2. AIJ

The flexural bearing capacity of CFSTs is calculated by the Japanese AIJ code [37] based solely on the contribution of the steel tube, without considering the contribution made by the concrete. The ultimate resistance $M_{u,AIJ}$ can be expressed as Eq. 20:

$$M_{u,AIJ} = C_b Z_x f_y \quad (20)$$

where C_b is the moment-gradient factor, and its value for a central point load applied on the simply supported beam can be taken as 1.35. f_y and Z_x represent the yield strength of the steel and the plastic section modulus about x-axis, respectively, determined as Eq. 21:

$$Z_x = \frac{bh^2}{4} - \frac{(b-2t)(h-2t)^2}{4} \quad (21)$$

where b , h and t represent the width, height, and thickness of the square steel tube, respectively.

5.3. AISC-LRFD and EN1994-1-1

The design moment resistance $M_{u,EC4}$ is determined by plastic theory which adopts a full plastic stress distribution in the composite section. The stress of steel tube in tension or compression is taken as yield stress f_y , and the stress of concrete is assumed to be $0.85f_{cd}$, while the concrete stress under tension is ignored. Accordingly, the design rules by EC4 [39] for bending resistance are the same as those of the compact sections implemented in the AISC [38]. According to the width-to-thickness ratio of the compression steel elements in composite members, AISC-LRFD [38] divides composite members subjected to bending into three types: compact, noncompact, and slender. The joints considered in this paper are compact and noncompact sections, whose bending capacity for CFST, $M_{u,AISC}$, can be expressed by Eq. 22 and Eq. 23, respectively:

(a) For compact sections:

$$M_{u,AISC} = M_p \quad (22)$$

where M_p is the moment corresponding to plastic stress distribution over the composite cross-section. M_p could be determined by plastic stress distribution, assuming that steel components have reached a stress of f_y in either tension or compression, and concrete components in compression due to flexure have reached a stress of $0.85f'_c$, where f'_c is the specified compressive strength of concrete.

(b) For noncompact sections:

$$M_{u,AISC} = M_p - \left(M_p - M_y \right) \left(\frac{\lambda - \lambda_p}{\lambda_r - \lambda_p} \right) \quad (23)$$

where λ , λ_p and λ_r are the slenderness ratios [38], M_y is the yield moment corresponding to yielding of the tension flange and first yield of the compression flange. The capacity at first yield is calculated assuming a linear elastic stress distribution with the maximum concrete compressive stress limited to $0.70f'_c$ and the maximum steel stress limited to f_y . The $M_{u,AISC}$ value needs to consider the moment-gradient factor C_b under mid-span applied concentrated force, which is taken as 1.35. This is similar to EC4 [39], which employs the same approach.

5.4. BS ISO 16521

The method for determining the bending capacity $M_{u,BS}$ of a square CFST chord according to BS ISO 16521 [40] is given in Eq. 24:

$$M_{u,BS} = \gamma_m W_{sc1} f_{sc} \quad (24)$$

where f_{sc} is the design compressive strength of a single CFST chord, γ_m is the plastic development factor of the bending resistance and W_{sc1} is the section modulus of a single chord. For CFSTs with a square cross-section,

γ_m and W_{sc1} are expressed as given in Eq. 25 and Eq. 26, respectively:

$$\gamma_m = 1.04 + 0.48 \ln(\xi + 0.1) \quad (25)$$

$$W_{sc1} = \frac{B^3}{6} \quad (26)$$

where B is the outside width of the square CFST chord.

ξ is the confinement coefficient, which is calculated as:

$$\xi = \left(A_s f_y \right) / \left(A_c A_c f_{ck} \right) \quad (27)$$

In these equations, f_y and f_{ck} are the characteristic material strengths of the steel tube and the concrete infill, respectively and A_c is the strength adjustment coefficient.

5.5. Limit balance approach

A method for determining the ultimate moment capacity based on the limit balance theory was proposed by Diao et al. [22] and this is examined herein. The method is based on the balance of internal forces in the chord cross-section. The compressive and tensile forces acting on the mid-span cross-section of a CFDSST T-joint are depicted in Fig. 23. According to Eq. 28, the total horizontal forces in the cross-section compression and tension zones must be equal in this analysis.

$$N_{cc} + \gamma N_{o1} + N_{o2} + N_{i1} + N_{s1} = N_{i2} + N_{o3} + N_{o4} + N_{s2} + N_{s3} \quad (28)$$

where N_{cc} is the resultant compressive force of concrete; N_{o1} and N_{o4} are the compressive force in the upper flange of the outer steel tube and the tensile force in the lower flange, respectively; N_{o2} and N_{o3} are the compressive and tensile forces in the web plates of the outer steel tube, respectively; N_{i1} and N_{i2} are the resultant forces on the compressed zone and the tensile zone on the inner steel tube, respectively; N_{s1} , N_{s2} , N_{s3} are the resultant forces in the stiffeners in the compressed zone and tensile zone, respectively; and γ is a reinforcement coefficient. Using the limit balance theory, the moment capacity $M_{u,LBT}$ of the CFDSST-to-SHS T-joint is computed as:

$$M_{u,LBT} = M_{cc} + M_{o1} + M_{o2} + M_{i1} + M_{s1} + M_{i2} + M_{o3} + M_{o4} + M_{s2} + M_{s3} \quad (29)$$

where M_{cc} is the moment capacity of concrete in compression; M_{o1} and M_{o2} are the moment capacities of the outer steel tube in compression zones, and M_{o3} , M_{o4} are in tension zones; M_{i1} and M_{i2} are the moment capacities of the inner steel tube in compression and tension zones, respectively; and M_{s1} , M_{s2} , and M_{s3} are the moment capacities of the stiffeners. These moment capacities are derived by multiplying the individual forces (from Eq. 28) by their respective distances from the neutral axis in Fig. 23. Thereafter, Eq. 29 can be expanded to Eq. 30 and by solving Eq. 28 and Eq. 30 simultaneously, the bending moment capacity $M_{u,LBT}$ is obtained as:

$$\begin{aligned} M_{u,LBT} = & M_{cc} + M_{o1} + M_{o2} + M_{i1} + M_{s1} + M_{i2} + M_{o3} + M_{o4} + M_{s2} + M_{s3} \\ = & \frac{1}{2} f_{cc} \left(B_0 - 2t_0 \right) x^2 + \gamma \sigma_{iv} B_0 t_0 \left(x + \frac{1}{2} t_0 \right) + \sigma_{iv} t_0 x^2 + \sigma_{iv} t_2 \left[B_2 \left(x - l - \frac{1}{2} t_2 \right) \right. \\ & \left. + (x - l - t_2)^2 \right] \\ & + 2\sigma_{iv} t_0 \left(h_s - t_0 \right) \left(x - \frac{1}{2} h_s + \frac{1}{2} t_0 \right) + f_y t_0 (B_0 - 2t_0 - x)^2 + f_y B_0 t_0 \\ & \left(B_0 - \frac{3}{2} t_0 - x \right) \end{aligned}$$

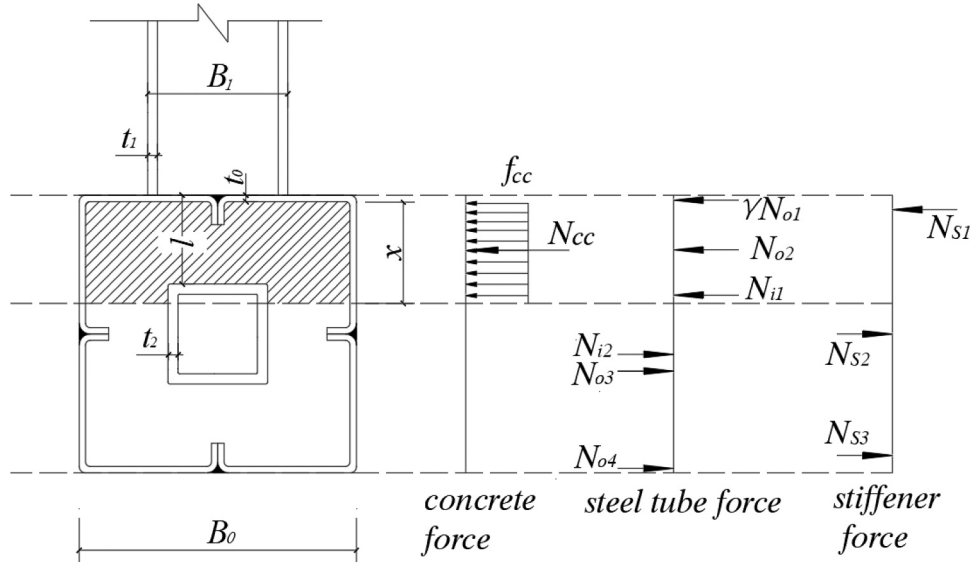


Fig. 23. Compression and tensile forces in the cross-section at mid-span.

$$\begin{aligned}
 & + f_y t_2 \left[(B_2 - x + l) (B_2 - t_2 - x + l) + B_2 \left(B_2 - \frac{1}{2} t_2 - x + l \right) \right] + 4 f_y t_0 \\
 & \left(h_s - t_0 \right) \left(\frac{1}{2} B_0 - t_0 - x \right) \\
 & + 2 f_y t_0 \left(h_s - t_0 \right) \left(B_0 - \frac{3}{2} t_0 - x - \frac{1}{2} h_s \right) - \frac{1}{2} f_{cc} (B_2 - 2 t_2) (x + t_0 - l - t_2)^2
 \end{aligned} \quad (30)$$

The brace reinforcement and confinement to the concrete in the compression zone are two crucial factors that affect the bearing capacity of CFDSST-to-SHS T-joints in the method. The strength of confined concrete (f_{cc}) and the reinforcement coefficient (γ) are used to quantify these two factors, where γ is determined using Eq. 31:

$$\gamma = 1 + 1.5 \beta \tau^{0.5} \quad (31)$$

where β equals B_1/B_0 as given before and $\tau = t_1/t_0$, with t_1 and t_0 representing the thicknesses of the brace and the chord, respectively. This coefficient effectively enhances the confinement effect of the brace on the chord, especially at the top flange, and amplifies the load-bearing capacity of the joint. The more reinforcement provided by the brace, the greater the value of γ .

The second key factor is the confinement effect on the concrete in the

compression zone of the chord. Diao et al. [22] adopt the approach proposed by Mander et al. [41] to calculate the strength of confined concrete (f_{cc}) which considers the confining forces applied by the surrounding steel and brace reinforcement. The strength of confined concrete can be calculated using Eq. 32:

$$f_{cc} = f_c \left(-1.254 + 2.254 \sqrt{1 + (7.94 f_l / f_c)} - 2 f_l / f_c \right) \quad (32)$$

where f_c is the characteristic compressive strength of concrete determined as $f_c = 0.4 f_{cu}^{7/6}$; f_l is the effective confining stress of concrete in compression zone given by $f_l = k_e f_i$; and k_e is calculated as $k_e = A_{ce}/A_c = (A_c - A_{cv})/A_c$. On the other hand, A_c , A_{ce} and A_{cv} represent different zones within the compression region of the concrete, which directly influence the load-bearing capacity of the joint including the area of concrete in the compression zone, the area of effectively confined concrete and the area of ineffectively confined concrete, respectively, as shown in Fig. 24. The latter is determined as $A_{cv} = 2 \times w_i^2/6$, where w_i is the width of the effectively confined region.

It is noteworthy that the effectiveness of the confinement reduces toward the sides, where the chord steel tube's side walls provide less confinement, as noted by the weaker confinement effect on these portions of the concrete. The distinction between these areas helps to assess the contribution of different parts of the concrete more accurately to the bearing capacity of the CFDSST-to-SHS T-joint. The reinforced brace increases the confinement effect, especially at the top of the concrete, leading to a stronger performance of the joint.

The solution of Eq. 32 requires the determination of the term f_l which is the lateral pressure of concrete, given from Eq. 33:

$$2 \sigma_{th} t_0 = f_l (B_0 - 4 t_0) \quad (33)$$

This expression assumes the distribution of equivalent stresses in the steel tube and confined concrete as shown in Fig. 25, noting that σ_{th} is the transverse stress of the steel tube wall.

It is possible to disregard the stress along the wall thickness direction by assuming that the steel tube and stiffeners are in a plane stress state, as suggested by Sakino et al. [42] and Zhou et al. [43]. Ge and Usami [44] state that when the ultimate bending capacity of a steel plate is reached, local buckling can be disregarded if $\frac{B_0}{t_0} \leq 1.7 \sqrt{\frac{E_s}{f_y}}$. Therefore, the transverse stress σ_{th} and the longitudinal stress σ_{tv} in the steel tube are taken as $0.19 f_y$ and $0.89 f_y$, respectively.

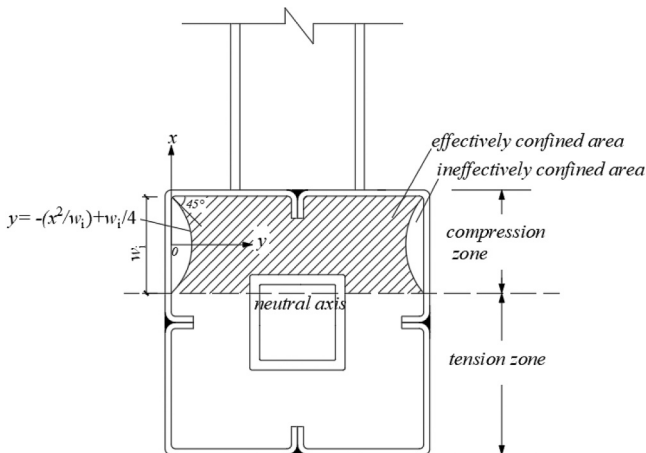


Fig. 24. Effectively-confined area of concrete.

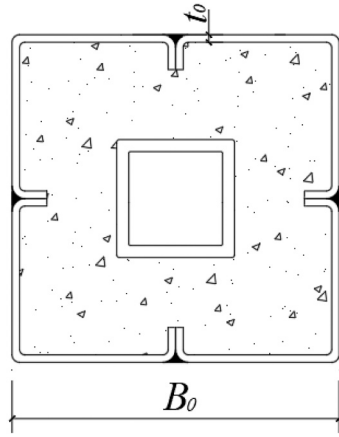


Fig. 25. Equivalent stress of steel tube and confined core concrete.

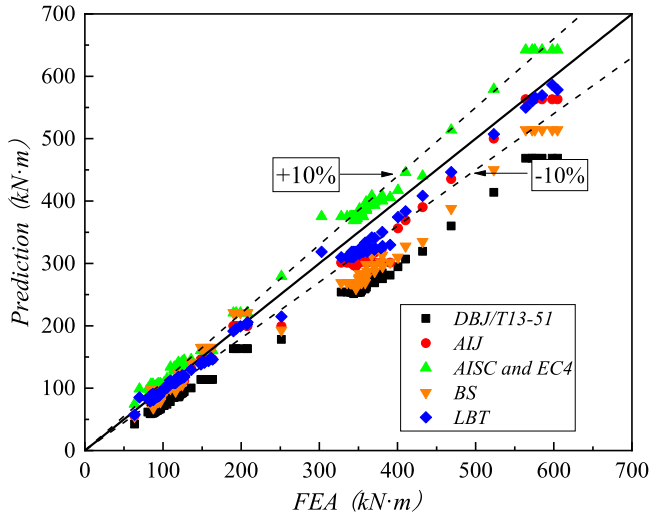
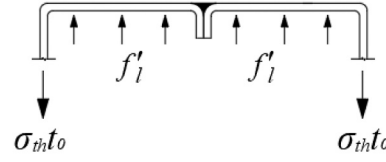


Fig. 26. Comparison of the design and numerical moment capacity predictions.

It is noteworthy that the design model described in the current section, using the limit balance theory, highlights the applicability of CFDSST elements for other applications as well as trusses.

5.5.1. Comparison between numerical and design capacities

This section compares the flexural bearing capacities predicted by the previously mentioned design methods and specifications (i.e., $M_{u,DBJ}$, $M_{u,AISC}$, $M_{u,AIJ}$, $M_{u,BS}$ and $M_{u,LBT}$) with the ultimate bending moments from the FE models (M_u^{FE}), as shown in Fig. 26 and summarised in Table 6. Using underlying mechanics, the relationship between the ultimate capacity (N_u^{FE}) and the ultimate bending moment (M_u^{FE}) is given as Eq. 34:

$$M_u^{FE} = N_u^{FE} L / 4 \quad (34)$$

It is evident from the comparisons that the standard deviation of the ratio between the design moments the numerical simulations for each method is relatively small, indicating consistent results across models. The average $M_{u,DBJ}/M_u^{FE}$, $M_{u,AIJ}/M_u^{FE}$, $M_{u,AISC}/M_u^{FE}$, $M_{u,BS}/M_u^{FE}$ and $M_{u,LBT}/M_u^{FE}$ ratios are 0.73, 0.92, 1.11, 0.89 and 0.95, respectively, and the corresponding standard deviations are 0.034, 0.058, 0.060, 0.098 and 0.041, respectively. As can be noticed, the results of AISC-LRFD [38]/Eurocode 4 [39] are higher than the FE predictions, which is unconservative.

The DBJ approach tends to underestimate the flexural bearing ca-

pacities of the CFDSST chord members, as evidenced by the lower average ratio of bending moment. This conservative prediction indicates that the method of DBJ is not ideal for calculating the flexural bearing capacity of CFDSST-to-SHS T-joints, because it depends on the severe uniform bending moment condition through ignoring the moment-gradient factor (C_b). AIJ [37] and the proposed limit balance theory provide the most accurate prediction of the flexural bearing capacity, as demonstrated by the average ratio of 0.93 and 0.95, respectively. With a comparatively low standard deviation of 0.041, limit balance theory ($M_{u,LBT}$), however, is the most accurate in terms of the FE model's results because it considers key elements that the other approaches do not, such as the brace reinforcement, confinement effect, and effective pressure area in the compression zone. Furthermore, the limit balance theory does not require consideration of the moment gradient coefficient C_b and can provide more accurate estimations than the methods in AIJ [37], AISC-LRFD [38], and Eurocode 4 [39], which consider the impact of various load modes on the bending moment bearing capacity through the value of C_b .

6. Conclusions

The structural behaviour of concrete-filled dual steel stiffened tube (CFDSST)-to-square hollow section (SHS) T-joints under axial loading was examined in this work, with emphasis on the joint capacity and associated failure modes. In order to evaluate the key factors influencing the behaviour, detailed finite element models were firstly established and validated, and subsequently followed by several parametric assessments. The key findings from this research are summarised in the points listed below.

1. To enable an assessment of the governing failure modes, a parameter K , defined as the flexural stiffness-to-length ratio of the brace relative to the chord, was suggested. The detailed results indicated that the boundary between the two main underlying failure modes, related to the brace or chord member, occurs at a value of K of 0.18.
2. The parametric assessments covered the key factors influencing the behaviour, including the material properties, geometric parameters, and axial force in the chord. It was shown that the brace-to-chord width ratio β ($\beta = B_1/B_0$) and thickness ratio τ ($\tau = t_1/t_0$) both increase the ultimate load capacity, with β having a larger influence on the ultimate capacity compared to τ .
3. In terms of material characteristics, the ultimate load capacity was found to be significantly influenced by the sandwiched concrete strength, particularly for larger cross-sections, while the core concrete strength does not have a notable effect. Further evidence that steel strength has a greater influence than concrete strength arises

from the fact that an increased steel strength significantly improves the load capacity, especially for larger chord sections.

4. It was shown that the axial forces in the chord decreased the T-joint ultimate load capacity. This effect became more noticeable as the axial load approached 0.6 times the chord ultimate axial load capacity. Additionally, yielding in the chord compression zone was shown to be accelerated by the presence of axial load.
5. The bearing capacity of the CFDSST-to-SHS T-joint with the two distinct failure modes was determined using the K -based division. The resistance value of the brace, N_b , can be used to calculate the bearing capacity of the CFDSST-to-SHS T-joint when $K < 0.18$. The bending capacity of the CFDSST chord determines the bearing capacity of the CFDSST-to-SHS T-joint when $K \geq 0.18$. By comparing the results obtained from international codes with the FE ones, it demonstrated that AIJ offered the most accurate estimation for the bending capacity of the CFDSST chord.
6. The limit balance theory was found to yield the most accurate predictions for the strength of joints with $K \geq 0.18$, whilst the AIJ [37] method also provides reasonable results.

Overall, the results show that, because of their distinct structural behaviour in comparison to conventional CFST joints, CFDSST-to-SHS T-joints offer several merits in terms of performance and application. Hence, they can be used to provide an efficient and effective solution in large-scale, heavily loaded structural engineering projects. The findings provide detailed insights into the main behavioural characteristics and strength predictions obtained by different international codes that can be used in practical assessment and design.

Author statement

The authors would like to confirm that we have all had a significant role in each of the following aspects of producing this article:

- The conception and design of the study, or acquisition of data, or analysis and interpretation of data.
- Drafting the article or revising it critically for important intellectual content.
- Final approval of the version to be submitted.

CRediT authorship contribution statement

Diao Yan: Validation, Methodology, Investigation, Formal analysis, Data curation, Conceptualization. **Wang Jun:** Writing – original draft, Validation, Resources, Methodology, Investigation, Formal analysis, Data curation, Conceptualization. **He Hongzhi:** Writing – original draft, Resources, Methodology, Investigation, Formal analysis. **Hassanein MF:** Conceptualization, Data curation, Formal analysis, Funding acquisition, Investigation, Methodology, Supervision, Visualization, Writing – original draft, Writing – review & editing. **Shao Yong-Bo:** Writing – review & editing, Validation, Supervision, Resources, Investigation, Funding acquisition. **Cashell Katherine Ann:** Writing – review & editing, Visualization, Validation, Methodology, Investigation, Formal analysis, Data curation. **Elghazouli A.Y.:** Writing – review & editing, Validation, Supervision, Methodology, Investigation.

Declaration of Competing Interest

The authors declare that they have no known competing financial interests or personal relationships that could have appeared to influence the work reported in this paper.

Acknowledgements

The research is sponsored by the Sichuan Natural Science Foundation (2024NSFC0163). The corresponding author also acknowledges

the support from the Xihua University Talent Introduction Fund No. Z241152.

Data Availability

Data will be made available on request.

References

- [1] Han LH, Li W, Bjorhovde R. Developments and advanced applications of concrete-filled steel tubular (CFST) structures: members. *J Constr Steel Res* 2014;100: 211–28.
- [2] Shanmugam NE, Lakshmi B. State of the art report on steel–concrete composite columns. *J Constr Steel Res* 2001;57(10):1041–80.
- [3] L.H. Han, Z. Tao, Design codes and methods on concrete-filled steel tubular structures in China, Proceedings of the International Symposium on Worldwide Trend and Development in Codified Design of Steel Structures, Singapore, 2006, pp. 46–74.
- [4] M.X. Xiong, D.X. Xiong, J.Y. Richard Liew, Axial performance of short concrete filled steel tubes with high-and ultra-high-strength materials, *Eng. Struct.* 136.
- [5] Tao Z, Han LH, Wang DY. Experimental behaviour of concrete-filled stiffened thin-walled steel tubular columns. *Thin-Walled Struct* 2007;45(5): 517–527. (2017) 494–510.
- [6] Guo JH, Diao Y. Experimental behaviors of square concrete filled steel tubular columns with PBL stiffeners. *Structures* 2022;38:1556–69.
- [7] Ekmekyapar T, Al-Eliwi BJM. Concrete filled double circular tube (CFDCST) stub columns. *Eng Struct* 2017;135(0):68–80.
- [8] Zhang JH, Shao YB, Hassanein MF. Axial compressive performance of ultra-high strength concrete-filled dual steel tubular short columns with outer stiffened tubes and inner circular tubes. *J Constr Steel Res* 2023;203:107848.
- [9] ACT-partner, advanced construction technology column, Accessed 21 August 2019, (<http://actpartner.co.kr>).
- [10] Ayough P, Ramli Sulong NH, Ibrahim Z. Analysis and review of concrete-filled double skin steel tubes under compression. *Thin-Walled Struct* 2020;148:106495.
- [11] Han L-H, Lam D, Nethercot D. Design Guide for Concrete-filled Double Skin Steel Tubular Structures. CRC Press; 2018.
- [12] Shi Y-L, Ji S-H, Wang W-D, W. X, Fan J-H. Axial compressive behaviour of tapered CFDCST stub columns with large void ratio. *J Constr Steel Res* 2022;191:107206.
- [13] Pons D, Ana Espinós, Alberio V, Romero ML. “Numerical study on axial loaded ultra-high strength concrete-filled dual steel columns”. *Steel Compos Struct* 2018; 26(6):705–17.
- [14] Wan CY, Zha XX. “Nonlinear analysis and design of concrete-filled dual steel tubular columns under axial loading”. *Steel Compos Struct* 2016;20(3):571–97.
- [15] Alberio V, Ibañez C, Piquer A, Hernández-Figueirido D. “Behaviour of slender concrete-filled dual steel tubular columns subjected to eccentric loads”. *J Constr Steel Res* 2021;176(0):106365.
- [16] Romero ML, Espinós A, Portolés JM, Hospitaler A, Ibañez C. “Slender double-tube ultra-high strength concrete-filled tubular columns under ambient temperature and fire”. *Eng Struct* 2015;99:536–45.
- [17] Wang ZB, Tao Z, Yu Q. “Axial compressive behaviour of concrete-filled double-tube stub columns with stiffeners”. *Thin-Walled Struct* 2017;120:91–104.
- [18] Zhang JH, Shao YB, Hassanein MF, Patel VI. “Axial compressive performance of ultra-high strength concrete-filled dual steel tubular columns with outer stiffened tubes and inner circular tubes”. *J Constr Steel Res* 2023;203:107848.
- [19] Wang ZB, Gao YH, Chi SY, Huang JZ. Stability of composite concrete-filled square thin-walled steel tubular slender columns under axial compression. *J Build Struct* 2017;38(12):41–8 ([in Chinese]).
- [20] Zhang JH, Shao YB, Hassanein MF, Cashell KA, Hadzima-Nyarko M. “Behaviour of ultra-high strength concrete-filled dual-stiffened steel tubular slender columns”. *Eng Struct* 2024;300:117204.
- [21] Wang ZB, Wei FB, Chi SY, Yu X. Study on behaviour of composite concrete-filled square thin-walled steel tubular columns under eccentric compression. *J Hunan Univ* 2018;45(9):43728.
- [22] Diao Yan, Qin Yi, Jiahao G. Experimental investigation on flexural performance of T-joint concrete-filled steel tube with PBL. *J Constr Steel Res* 2023;204.
- [23] Yang YF, Bie XM, Fu F. Static performance of square CFDCST chord to steel SHS brace T-joints. *JCSR* 2021;183:106726.
- [24] Li K, Yu SH, Feng WJ. The parametric analysis on ultimate bearing capacity for T-type joints made of rectangular concrete-filled steel tubular. *J Anhui Inst Archit Ind* 2011;19(3).
- [25] Ma YP, Liu YJ, Wang K, et al. Axial stiffness of concrete filled rectangular steel tubular (CFRST) truss joints. *JCSR* 2021;184:106820.
- [26] ABAQUS, ABAQUS Standard User’s Manual, Version 2020, Dassault Systèmes Corp, Providence (RI, USA), 2020.
- [27] Tao Z, Wang ZB, Yu Q. Finite element modelling of concrete-filled steel stub columns under axial compression. *J Constr Steel Res* 2013;89:121–31.
- [28] GB 50017-2017. Standard for design of steel structures. Beijing: China Building Industry Press; 2017.
- [29] Hassanein MF, Shao Yong-Bo, Zhang Jun-Hua, Cashell KA, Elsisy AR. Global buckling behaviour and design of square cold-formed concrete-filled dual steel stiffened slender columns. *J Constr Steel Res* 2024;218:108706.
- [30] Zhang Jun-Hua, Hassanein MF, Cashell KA, Hadzima-Nyarko Marijana, Xu Yang, Shao Yong-Bo. Experimental and numerical investigation on the behaviour of

- square concrete-filled cold-formed double-skin steel stiffened tubular short columns. *Eng Struct* 2024;303:117560.
- [31] Zhang JH, Shao YB, Hassanein MF, Cashell KA, Hadzima-Nyarko M. "Behaviour of cold-formed concrete-filled dual steel stiffened tubular short columns". *J Constr Steel Res* 2024;213:108381.
- [32] Yukai Wang. Research on the mechanical performance of T-joint concrete-filled steel tube with PBL. Master'S Thesis Xihua Univ 2024;7 (in Chinese).
- [33] DBJ/T13-51-2010. Technical Specification for Concrete-Filled Steel Tubular Structures. Fuzhou, China: The Construction Department of Fujian Province; 2010.
- [34] Cai SH. Concrete filled steel tubular structures. Beijing, China: China Communications Press; 2003 (in Chinese).
- [35] Bock M, Gupta S, Hassanein MF, Sheng Y. "A slenderness based method for web crippling design of aluminium tubular sections". *J Struct Eng, ASCE* 2022;148(12): 04022205.
- [36] NAS (North American Specification). North American specification for the design of cold-formed steel structural members. Washington, DC: American Iron and Steel Institute; 2001.
- [37] Architectural Institute of Japan. Recommendations for design and construction of concrete filled steel tubular structures: AIJ-CFT 2008) [S]. Tokyo: Architectural Institute of Japan, 2008.
- [38] American Institute of Steel Construction (AISC). Load and resistance factor design (LRFD) specification for structural steel buildings, Chicago; 2010.
- [39] Eurocode 4. Design of Composite Steel And Concrete Structures. BS EN 1994-1-1: 2004. British Standards Institution; 2004.
- [40] BS ISO 16521: 2024. Design of concrete-filled steel tubular (CFST) hybrid structures, ISBN 978 0 539 24548 6, 2024.
- [41] Mander JB, Priestley MJN, Park R. Theoretical stress-strain model for confined concrete. *J Struct Eng* 1988;114(8):1804–26.
- [42] Sakino K, Nakahara H, Morino S, et al. Behavior of centrally loaded concrete-filled steel-tube short columns. *J Struct Eng* 2004;130(2):180–8.
- [43] Zhou Z, Gan D, Zhou XH. Improved composite effect of square concrete filled steel tubes with diagonal binding ribs. *J Struct Eng ASCE* 2019;145(10):04019112.
- [44] Ge HB, Usami T. Strength of concrete-filled thin-walled steel box column: experiment. *J Struct Eng ASCE* 1992;118(11):3036–54.